Progress In Electromagnetics Research, Vol. 166, 119–145, 2019

Modulation on Silicon for Datacom: Past, Present, and Future

Binhao Wang[1], Qiangsheng Huang[2], Kaixuan Chen[2], Jianhao Zhang[2], Geza Kurczveil[1], Di Liang[1], Samuel Palermo[3], Michael R. T. Tan[1], Raymond G. Beausoleil[1], and Sailing He[2, *]

(*Invited Review*)

Abstract—Datacenters become an important part of technical infrastructure. The Datacom traffic grows exponentially to satisfy the demands in IT services, storage, communications, and networking to the growing number of networked devices and users. High bandwidth and energy efficient optical interconnects are critical to improve overall productivity and efficiency in data centers. Mega-data centers are expected to address the power consumption and the cost in which optical interconnects contribute quite a large part. Silicon photonics is a promising platform to offer savings in power and potential increase in bandwidth for Datacom. Several modulation techniques are developed in silicon photonics to reduce the optical mode volume or enhance the light matter effect to further improve the modulation efficiency. Many other materials such as III-V and $LiNbO_3$ are integrated on silicon photonics to maximize the optical link performance. This paper reviews several modulation techniques for Datacom, from vertical-cavity surface-emitting laser (VCSEL) direct modulation to silicon photonics modulators then to hybrid silicon modulators.

1. INTRODUCTION

The Datacom traffic has grown tremendously due to the cloud computing and applications in video streaming, Artificial Intelligence (AI), and Internet of Things (IoT). The large amount of data demands mega-data centers with high bandwidth and energy efficient optical interconnects. Currently vertical-cavity surface-emitting laser (VCSEL) based interconnects are the simplest, most power efficient and cost-effective optical links for Datacom. However, bandwidth and distance scaling are limited due to the discrete components and multimode transmission. To extend the transmission distance, single-mode long-wavelength VCSELs are being investigated which require epitaxial regrow with buried tunnel junction (BTJ) and suffer less index contrast distributed Bragg reflectors (DBRs) [1]. It results in more complicated fabrication and lower modulation speed. Indium phosphide (InP) is a favorable platform due to the high integration and the complete functionality for building components, including lasers, modulators, photodiodes, couplers, and wavelength (de)multiplexers. Directly modulated distributed feedback lasers (DFBs) or electroabsorption (EA) DFBs in InP platform have been demonstrated for 400 GbE [2]. However, the fragile nature of InP has difficulties to scale the wafer size, and the complementary metal-oxide-semiconductor (CMOS) noncompatibility for InP platform may result in not low enough cost for applications in mega-data centers.

Silicon photonics is an alternative attractive platform due to its CMOS compatibility and high integrability [3]. Key components except laser sources have been developed in silicon photonics.

Received 24 October 2019, Accepted 15 December 2019, Scheduled 23 December 2019

* Corresponding author: Sailing He (sailing@zju.edu.cn).

[1] Hewlett Packard Labs, Hewlett Packard Enterprise, 1501 Page Mill Rd, Palo Alto, CA 94304, USA. [2] Centre for Optical and Electromagnetic Research, National Engineering Research Center for Optical Instruments, Zijingang Campus, Zhejiang University, Hangzhou 310058, China. [3] Analog and Mixed-Signal Center, Texas A&M University, College Station, TX 77840, USA.

Heterogeneous integration has been investigated to resolve the laser source bottleneck which enable complete functionality in silicon photonics platform [4]. The plasma dispersion effect based silicon photonics Mach-Zehnder (MZ) modulators at data rate of $> 100\,\mathrm{Gb/s}$ have been demonstrated [5]. However, the weak silicon plasma dispersion and free carrier absorption in silicon cause the low modulation efficiency, resulting in a device length of around a few millimeter for MZ modulators. Many efforts have been investigated to improve the modulation efficiency and reduce the device footprint. High quality-factor cavity assisted silicon modulators using resonators have been proposed which tremendously reduce the modulator size to $< 10\,\mu\mathrm{m}$ diameter [6]. Compared to conventional silicon MZ modulators, slow-wave effect based photonic crystal silicon modulators with more than $10\times$ smaller size have been demonstrated [7]. Surface plasmon-polaritons (SPP) based modulators have attracted due to the strong optical confinement [8]. However, they usually suffer high insertion loss. Hybrid silicon modulators, e.g., III-V on silicon and $LiNbO_3$ on silicon, based on quantum-confined Stark effect (QCSE) [9], plasma dispersion effect, or Pockels effect [10] using heterogeneous integration are also being investigated to enhance the modulation efficiency or the bandwidth.

Besides the work on improving device performance, other techniques such as advanced modulation scheme (e.g., four-level pulse amplitude modulation (PAM4)), analog coherent modulation [11], wavelength division multiplexing (WDM) or space division multiplexing (SDM) [12] are utilized to increase the Datacom bandwidth. In this paper, we review several modulation techniques for Datacom, from VCSEL direct modulation to silicon photonics modulators then to hybrid silicon modulators. The paper is organized as follows: Section 2 discusses VCSEL interconnects. Silicon photonics modulators, including Mach-Zehnder modulators, microring modulators, and photonic crystal modulators, are reviewed in Section 3. Section 4 reviews hybrid silicon modulators in which electroabsorption modulators and electro-optic modulators are discussed and compared. A discussion about all different types of modulators is presented in Section 5. Finally, Section 6 concludes the paper.

2. VERTICAL-CAVITY SURFACE-EMITTING LASERS

Currently VCSEL based interconnects are the simplest and most widely deployed short-reach optical links. These are based on directly modulated 850 nm VCSEL/photodiode (PD) arrays operating at 25/50 Gb/s coupled to multimode fiber using low cost injection molded micro-optics. Most high performance computing (HPC) systems or data centers today utilize these links in the form of parallel optical modules, active optical cables or industry standard pluggable optical transceivers. Unlike its Telecom counterpart, there has been little progress in the use of multiple wavelengths in VCSEL based optical links. In recent years, shortwave wavelength division multiplexing (SWDM) VCSEL links with wavelengths at 850 nm, 880 nm, 910 nm, and 940 nm have been demonstrated which achieved 4×50 Gb/s non-return-to-zero (NRZ) signaling over a 50 m OM4 multimode fiber [13]. VCSELs in the 1000 nm wavelength range are attractive due to their high speed performance over temperature and simple flip-chip reflowed assembly [14]. A 4×6 coarse WDM (CWDM) transmitter/receiver (Tx/Rx) optical module based on this technology has been demonstrated with an aggregate throughput of more than 1 Tb/s [15].

A schematic of the VCSEL based co-packaged CWDM optical module is shown in Fig. 1. Bottom emitting VCSELs (990, 1015, 1040, and 1065 nm) were chosen due to the ease with which they can be flip-chip solder reflowed onto the printed circuit board (PCB) substrate. The integration of a collimating lens on the VCSELs eliminate the need for a separate optical element along with the additional serial alignment process step. The collimated output beam from the lensed VCSEL improve the lateral alignment tolerance to the zig-zag multiplexer/demultiplexer (Mux/DeMux) assembly. The VCSELs are nominally of the same design with modifications to the DBR, oxide and quantum well layers to adjust for the emission wavelength range of over 75 nm. Strain compensation allows the use of highly strained InGaAs quantum wells resulting in higher differential gain and better over-temperature performance [16]. VCSEL optical spectra with CWDM filter transmission band is shown in Fig. 1(b). Good spectral alignment between the VCSELs and bandpass filters results in a low optical crosstalk of better than 35 dB between channels. A 25 nm channel spacing was chosen to allow for manufacturing variations of VCSELs and filters while removing the need for temperature control of the VCSEL wavelength, improving yield and reducing cost. For the receiver, a two dimensional (2D), lensed, bottom entry

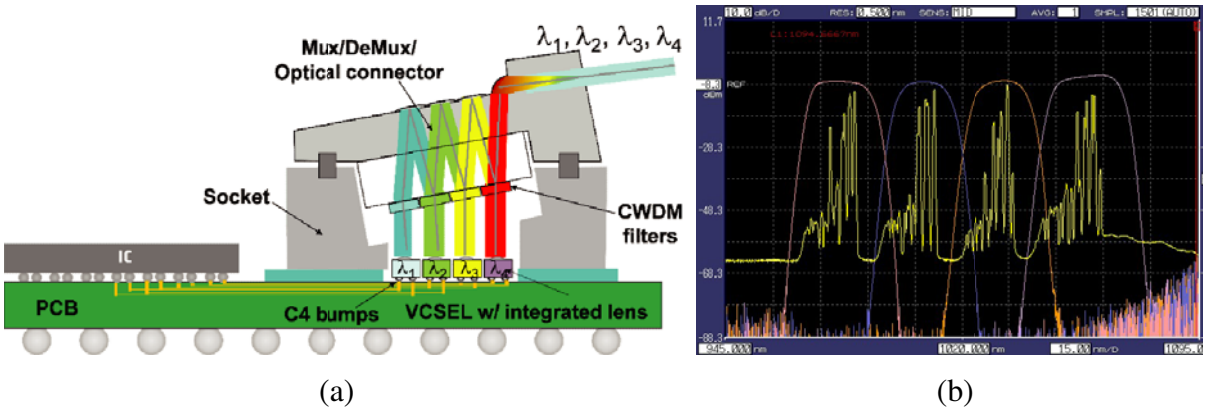

Figure 1. (a) Prototype co-packaged CWDM optical Tx/Rx module showing Mux/DeMux, OE array, IC, and output fiber; (b) VCSEL optical spectra with CWDM filter transmission band [15].

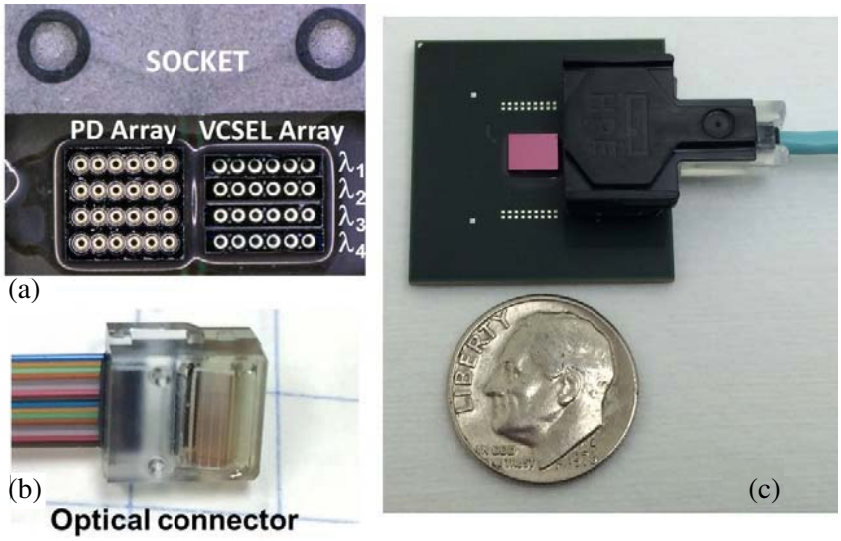

Figure 2. (a) PD and VCSEL arrays on organic substrate with socket, (b) an optical connector with Mux/De-mux, and (c) an assembled CWDM Tx/Rx module [15].

InGaAs p-i-n PD array is placed next to the VCSEL arrays.

Application-specific integrated circuit (ASIC) and optical input/output (I/O) co-package solution is the promising approach to scale the Datacom bandwidth capacity. This complete co-package solution is compatible with lead-free solder reflow processes allowing the direct integration of the co-package solution onto a PCB assembly without the need for a separate electrical connector. As shown in Fig. 2, the assembled CWDM optical module with a capacity of 1.2 Tb/s in a volume of about 1 cm^3. The co-package solution can be tiled horizontally around a switch chip to provide for a very high density multi-Terabit per second optical I/O.

Data rates and wavelengths are two dimensions to scale the VCSEL optical link capacity. Advanced modulation scheme, such as PAM4, has become IEEE standard for 400 Gb Ethernet. PAM4 signaling can double the data rates by sending two bits per symbol compared to NRZ. To increase the number of wavelength per fiber, multimode fiber (MMF) manufacturers have developed OM5 MMF to provide sufficient bandwidth from 850 to 950 nm. It has been shown that 100 Gb/s VCSEL PAM4 transmission across four wavelengths (850, 880, 910, 940 nm) is feasible in OM5 MMF [17]. To meet the demand of continual growth of Datacom, more wavelengths are needed to scale the VCSEL link capacity. Eight

wavelengths (850, 880, 910, 940, 970, 1000, 1030, 1060 nm) with 30 nm channel spacing over OM5 MMF are being investigated. Error-free 100 Gb/s PAM4 transmission over 100 m OM5 MMF using two-end wavelength (850 and 1060 nm) VCSELs has been successfully demonstrated [18]. However, eight wavelength Mux/DeMux using dielectric filters will be a challenge due to the required angle and x-y alignment over eight wavelengths. Photonic integrated circuits (PIC) on silica, silicon or Si_3N_4 have been demonstrated to achieve CWDM/DWDM with eight wavelengths or more using Mach-Zehnder interferometer (MZI) based lattice filters [19], arrayed waveguide gratings (AWG) [20], or Echelle diffraction gratings (EDG) [21]. How to integrate VCSEL on PIC with low loss is critical to scale the bandwidth capacity of VCSEL links.

Mega-data centers are a result of data center consolidation to minimize the operational cost and the power consumption. Numerous companies are moving toward mega-data centers to take advantages of reduced complexity, improved energy efficiency and simpler management infrastructure. Nowadays, VCSEL interconnects in high performance computers or data centers are based on 850 nm VCSEL/PD arrays coupled to MMF. However, the transmission distance is limited to 100–200 m with 850 nm multimode VCSELs. VCSEL link distance extension techniques have been investigated to extend the transmission distance to a few kilometers for mega-data centers. 1060 nm single-mode VCSELs over 2 km using single mode fibers have been demonstrated at 40 Gb/s NRZ [22] and 50 Gb/s PAM4 [23]. In addition, long-wavelength (1310/1550 nm) VCSELs have also attracted researchers' interest. More than 10 km transmission distance using long-wavelength VCSELs with 3 dB bandwidth of 17–18 GHz has been demonstrated [24, 25]. Typically, long-wavelength VCSELs using InP quantum wells are not able to use GaAs/AlGaAs DBRs which cannot utilize the oxidation process to confine the current flow and the optical modes. Instead, InP long-wavelength VCSELs require to grow buried tunnel junction (BTJ) and dielectric mirrors, or use regrown tunnel junction combined with wafer-fused GaAs/AlGaAs DBRs [26], which increase the complexity of the device fabrication. Dilute nitride (GaInNAs/GaAs) VCSELs are an alternative approach to realize long lasing wavelength [27]. The high speed performance still needs to be improved and the epitaxial grow using metal organic chemical vapor deposition (MOCVD) for massive production is also an ongoing challenge.

Compared to VCSEL interconnects, optical interconnects using external modulators are able to achieve higher data rates thanks to the simpler mechanism of modulators and longer transmission distance due to the single-mode operation and less frequency chirp. Moreover, moving from discrete components (e.g., VCSEL interconnects) to integrated platform (e.g., silicon photonics interconnects) can use DWDM or analog coherent optics to further scale the bandwidth capacity.

3. SILICON PHOTONICS MODULATORS

Silicon photonics modulators have been developed for more than a decade since the first breakthrough in the GHz modulation frequency on a silicon waveguide [28]. In order to meet the requirements of higher capacity and long-haul communications, big data applications and high-performance computing, etc., silicon photonics modulators are investigated to achieve higher modulation efficiency, larger bandwidth, lower loss, lower power consumption and complex modulation formats. As transceiver circuitry consumes the major power in an optical link, silicon photonics modulators with higher modulation efficiency play an important role for saving power consumption. Currently most silicon photonics modulators can achieve tens of GHz of electro-optic (EO) bandwidth benefited from the study of modulation mechanism, optimization of doping profile, precision process and design of driving electrode. Optical modulators are able to realize integration with driver circuits to reduce the package complexity and the cost as well as minimize electrical parasitics for short-reach or even on-chip optical interconnects. The monolithic integration of silicon photonics modulators with drivers in full digital electronics CMOS processes has been reported [29–31]. Silicon photonics modulators have been used in industrial transceiver modules for 100 and 400 Gb/s data center applications [32–34].

The properties of the light in silicon waveguides are mainly changed through the change of the refractive index of waveguides including real and imaginary parts. The two common methods to change the refractive index of silicon waveguides are based on the thermo-optic effect and the plasma dispersion effect. The thermo-optic effect is usually used in low-speed optical switches [35] or phase control driven by non-high-speed information [36]. The most high-speed silicon photonics modulators are operated

based on the plasma dispersion effect. The changes of index and absorption loss due to the change of free carriers are described by the classic Drude model [37]

$$\Delta n = \frac{-q^2\lambda_0^2}{8\pi^2 c^2 n\varepsilon_0}\left(\frac{\Delta N_e}{m_{ce}^*} + \frac{\Delta N_h}{m_{ch}^*}\right) \tag{1}$$

$$\Delta\alpha = \frac{-q^3\lambda_0^2}{4\pi^2 c^3 n\varepsilon_0}\left(\frac{\Delta N_e}{m_{ce}^{*2}\mu_e} + \frac{\Delta N_h}{m_{ch}^{*2}\mu_h}\right) \tag{2}$$

where q, c, ε_0, n, and λ_0 are the elementary electronic charge, speed of light in vacuum, permittivity of free space, unperturbed material refractive index, and light wavelength in vacuum, respectively. ΔN_e and ΔN_h are the respective concentration change of electrons and holes. Two material parameters, conductivity effective mass m_{ce}^*, m_{ch}^* and mobility μ_e, μ_h for electron and hole, respectively, differentiate the plasma dispersion effect in different materials.

Three common types of silicon photonic modulators [38], carrier-accumulation, carrier-injection, and carrier-depletion modulators, are shown in Fig. 3. Carrier-accumulation modulators (Fig. 3(a)) have a silicon oxide thin layer as an isolator in waveguides to form a capacitor. When the bias voltage increases, the number of free carriers on the capacitor increases as well as the effective index of the optical mode [39]. The carrier-accumulation modulators usually have high modulation efficiency, e.g., a voltage-length product $V_\pi L$ lower than 0.2 V·cm has been demonstrated in [40]. However, polysilicon deposition is often required for the fabrication of carrier-accumulation modulators, which results in high loss and not compatibility with SOI platform [40, 41]. Furthermore, high modulation efficiency stemmed from their large capacitance is also at the expense of the large RC time constant. In carrier-injection modulators (Fig. 3(b)), n-type and p-type doped regions are separated by intrinsic silicon which form a p-i-n diode. Carrier-injection modulators based on forward-biased p-i-n junctions are another alternative with high modulation depths and rapid bias-based resonance wavelength tuning capabilities [42, 43], but their speed is limited by both long minority carrier lifetimes and series resistance effects [44]. For carrier-depletion modulators (Fig. 3(c)), n-type and p-type doped regions are abutted in the waveguide which form a p-n diode. Carrier-depletion modulators are getting more popular due to their more straightforward fabrication process and flexible design, which is promising for high speed and high efficiency at the same time. More than 100 Gb/s data rate with $V_\pi L$ of 1.4 V·cm has been reported [45]. The modulators discussed in the following are based on carrier-depletion except for special instructions.

(a) (b) (c)

Figure 3. Cross section views of three silicon photonic modulators: (a) carrier accumulation, (b) carrier injection, and (c) carrier depletion.

Here are four metrics to describe the performance of silicon photonic phase shifters: modulation efficiency, modulation bandwidth, insertion loss, and power consumption per bit (energy efficiency). $V_\pi L$ with a unit of V·cm is a key parameter to describe the efficiency of phase shift which the required driving voltage applied on a 1 cm long phase shifter for a π phase change. Obviously, the larger capacitance C in the modulation region has a larger modulation efficiency. In addition, the power consumption per bit is $E_{bit} = CV^2/4$ [46], which has a linear relationship with the capacitance C but a square relationship with the voltage V. Therefore, the increase of the capacitance C may reduce the power consumption due to the reduced driving voltage V. The higher capacitance can be achieved by implanting higher doping concentration in the PN junction. However, higher doping concentration leads to larger free carrier absorption and consequently increases the light propagation loss in waveguides. Although the higher doping concentration results in lower series resistance, the modulation bandwidth limited by the RC time constant may or may not be affected, which depends on the PN junction design. Another way to improve the modulation efficiency and then reduce the power consumption is to increase the overlap

of the PN junction and the optical mode, which may increase the design and fabrication complexity. In general, the design of silicon optical phase shifters is necessary to consider the tradeoffs of these metrics.

3.1. Silicon Photonics Mach-Zehnder Modulators

The most popular type of silicon photonic modulators is based on Mach-Zehnder interferometers (MZI) which converts the change of the phase shifts of two arms into the change of the MZI output amplitude via constructive or destructive interference. The basic structure of doping regions in carrier-depletion phase shifter can be classified into three categories: vertical, horizontal and interdigital PN junction. As shown in Fig. 4(a), the vertical PN junction has a larger junction area, therefore, a larger capacitance compared to a horizontal PN junction (Fig. 4(b)) since the waveguide width is often designed to be larger than its height [47]. However, it requires top-contact electrodes and silicon regrow on the upper surface, which is not compatible with traditional rib waveguides. Although some doping techniques in vertical direction such as in situ doping [48] or alternating implantation and epitaxial overgrowth steps [49] have been proposed, the fabrication process is still complex. Most of researchers choose a horizontal PN junction in the center of the rib waveguide with the same width of P and N areas due to the straightforward fabrication process of the doping profiles, as shown in Fig. 4(b), which can achieve 40–50 Gb/s data rate with doping profile optimization [50, 51]. As shown in Fig. 4(c), the interdigitated PN junction has larger depletion area, which reduces the voltage-length product to 0.56 V·cm [52]. Furthermore, this type of PN junction has large tolerance to the junction misalignment [53]. These three types of PN junctions can be combined together to achieve low $V_\pi L$ and propagation losses as shown in Fig. 4(d) [54].

Due to the straightforward fabrication process and flexible doping profiles in horizontal PN junction, the performance of phase shifters using horizontal PN junction has been improved in terms of the modulation efficiency, the bandwidth, and the loss. Since the influence of p-type carrier concentration on refractive index is greater than that of n-type carrier concentration [37], the PN junction can have offset from the center of the waveguide to improve the modulation efficiency and reduce the loss as shown in Fig. 4(e). This structure has been used in many high-performance modulators assisted by other techniques such as self-aligned fabrication process [55], single-drive for push-pull [50] and doping concentration optimization [56]. Since most of the field energy is concentrated in the middle of the waveguide, doping in the non-intermediate region has little impact on the change of refractive index and only brings additional losses. As shown in Figs. 4(f) and 4(g), the doping concentration in these regions can be reduced or removed [57, 58], such as the PIPIN type junction (Fig. 4(f)) and reduced doping concentration in two corners of a rib waveguide (Fig. 4(g)). A PN junction fabricated by

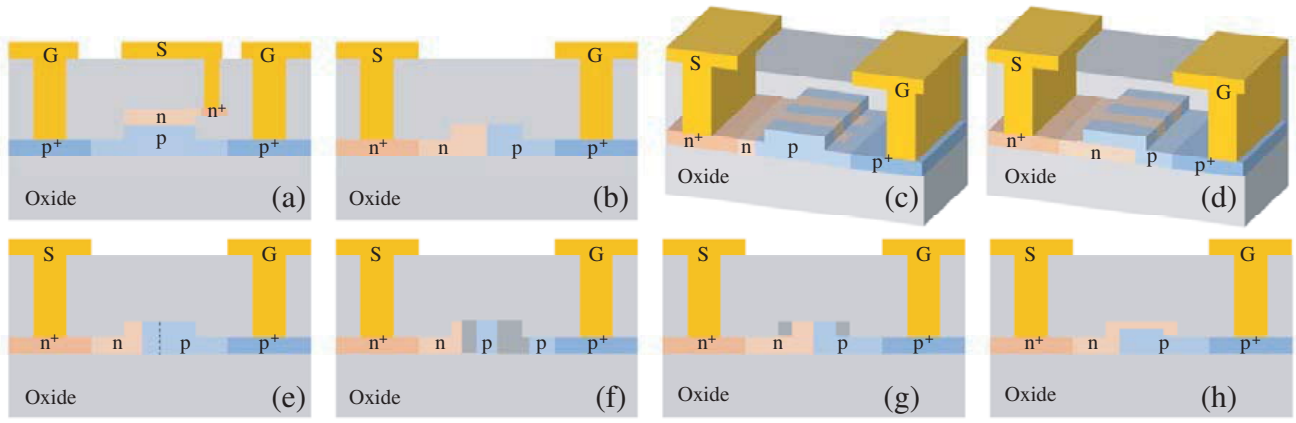

Figure 4. Schematics of the PN junctions in various silicon carrier-depletion modulators: (a) vertical PN junction, (b) horizontal PN junction, (c) interdigital PN junction, (d) combination of three types of PN junction, (e) horizontal PN junction with offset, (f) PIPIN junction, (g) reduced doping concentration in two corners and (h) angled implantations.

angled implantations was also proposed for polarization independence modulator [59] or high modulation efficiency [60], as shown in Fig. 4(h). Fabrication tolerance also needs to be considered in the design of a PN junction. The misalignment of the PN junction could affect the modulator performance since the most of the optical power is confined in the center of the waveguide [61]. The self-aligned process technique has been developed to achieve perfect alignment by defining the waveguide and implantation area in the same lithography step [55, 57]. Table 1 summarizes performances of MZ modulators with aforementioned typical doping profile techniques.

Table 1. Performance comparison of silicon photonics MZ modulators with different doping profiles.

Reference	Length (mm)	Data rate (Gbps)	ER (dB)	IL (dB)	V_{pp} (V)	$V_\pi L$ (V·cm)	Concentration (cm^{-3})	Technology
[62]	0.75	60	4.4	2	6	1.8	P: 2×10^{17} N: 2×10^{17}	Offset, precisely aligned
[57]	0.95	40	3.2	4.5	6	3.5	P: 3×10^{17} P+: 8×10^{17} N+: 10^{18}	PIPIN, self-aligned
[55]	1	50	3.1	7.4	6.5	2.8	P: 3×10^{17} N: 1.5×10^{18}	Offset, self-aligned
[50]	2	50	4.7	4.1	4.5	2.4	P: 5×10^{17} N: 5×10^{17}	Offset, single-drive push-pull
[58]	4	50.1	5.56	4.16	7	2.67	-	Corner compensated doping
[51]	3	50	3.4	3.34	1.5	2.43	P: 7×10^{17} N: 5×10^{17}	Horizontal, concentration optimization
[56]	0.75	50	7.5	6.5	6.5	2.05	P: 2×10^{17} N: 2×10^{17}	Offset, concentration optimization
[63]	3	50.5	7.08	9	3.5	1.85	P: 4×10^{17} N: 4×10^{17}	Corner compensated doping, Cu electrode
[64]	0.75	40	7.01	2	7	$1.5 \sim 2$	P: 2×10^{17} N: 2×10^{17}	Interleaved junctions
[61]	1.35	40	6.5	15	6	11(TE) 14(TM)	P: 1×10^{18} N: 1×10^{18}	Angle implantations, self-aligned

It should be noted that the analysis above focuses on phase shifters only. For a practical modulator, the total performance of the device needs to be considered. For example, the total power consumption per bit is also related to the output voltage of radio frequency (RF) signal source, the bias DC current and the termination of modulators. The bandwidth of modulators not only depends on the RC time constant but also relies on the design of the driving electrode. There are two typical designs for the driving electrode, the lumped electrode and the traveling wave electrode. The lumped electrode is used in the condition when a phase shifter is much shorter than the RF wavelength that does not need a termination to reduce the reflection. As a result, the power consumption of lumped electrodes is much smaller than that of traveling wave electrodes. Owing to the standing wave in lump electrodes, the driving voltage is half of that in the traveling wave electrode with the same size. The dynamic power consumption of the lumped electrode can be typically as small as a few to tens of fJ/bit when it applies to a microring modulator [65–67]. The traveling wave electrode is commonly used in the Mach-Zehnder modulator (MZM) with a long phase shifter. Usually a 50 Ohm termination resistance is required at the end of the traveling wave electrode to prevent RF signal reflection. The remaining voltage drop from the phase shifter will consume on the termination. The power consumption is proportional to the total driving voltage squared and inversely proportional to the impedance of the device and the data rate.

In addition, we also need to consider extinction ratio (ER), optical bandwidth, temperature stability, and package to make modulators practical. Compared to resonant type modulators, MZMs

have a larger size mainly consumed on the length of the phase shifter. Resonators with a smaller size such as rings or disks have lower drive voltage and lower power consumption [65–67] than MZMs. However, the high dependence on the wavelength of the resonator leads to the instability of machinery and temperature, and the extremely low working bandwidth (< 1 nm) will increase the burden of temperature control and light source control of the system. The optical bandwidth of MZMs is relatively large. For a symmetric MZM, it is not difficult to cover the whole O band or C band. Since the temperature changes in both arms compensate for each other, the temperature has little influence on MZMs.

Silicon photonics MZ modulators have been well developed over ten years, with the modulation speed up to dozen of Gb/s without complex modulation formats. Silicon photonics MZ modulators are expected to be used in next-generation datacenter optical networks, 5G optical modules and supercomputing to further speeding up the data rate, reducing the power consumption and the cost of the system. At present, engineers and academics are actively solving problems of its driver, packaging and coupling with the laser source in order to meet the requirements from the near future huge market [32–34].

3.2. Silicon Photonics Microring Modulators

High-speed modulators need to be energy efficient and ultra-compact, in order to satisfy the increasing data communication demands. As discussed in earlier study [68], the power consumption of a device, i.e., energy-per-bit, is proportional to V_{mode}/Q, where V_{mode} is the optical mode volume and Q is the cavity quality factor. To reduce the power consumption, we can either minimize the optical mode volume or take the advantage of a higher Q factor. The refractive-index change in silicon microring modulators enables the switching between on- and off-resonance states at a given wavelength detuning. Compared to MZ modulators, silicon microring modulators are more promising for high bandwidth density and energy efficiency (i.e., low power consumption) thanks to their small active volume and high Q factor. Two types of microring modulators will be discussed as below, carrier-injection and carrier-depletion microring modulators.

3.2.1. Carrier-injection Microring Modulators

As shown in Fig. 5(a), a carrier-injection microring modulator consists of a ring resonator side-coupled to a bus waveguide, with p+ and n+ doping in the inner and outer ring regions, respectively. A

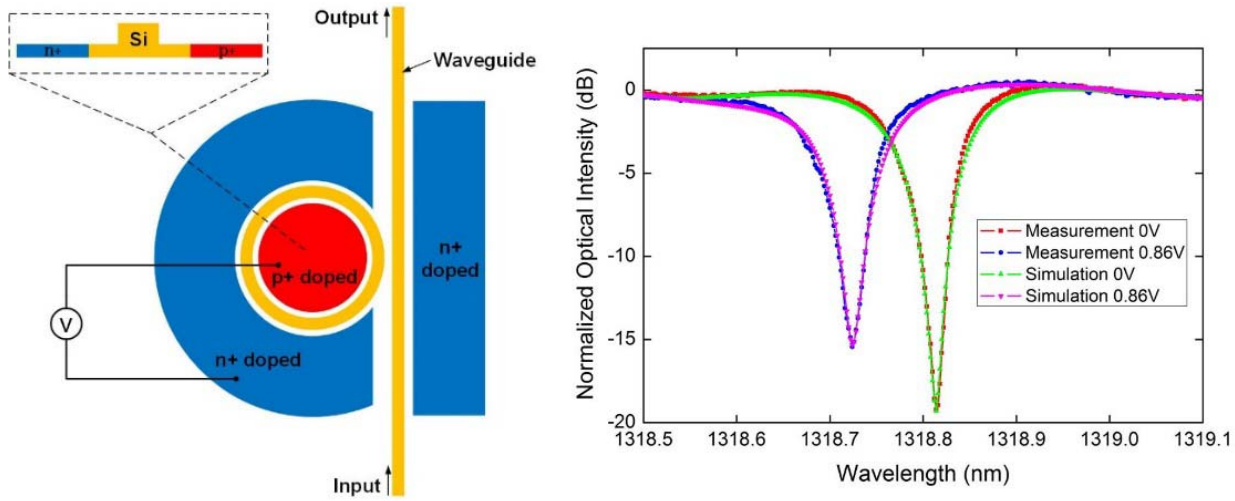

Figure 5. (a) Top and cross section views of a carrier-injection microring resonator modulator; (b) typical carrier-injection microring resonator spectral shift via applied voltage [69].

compact model for carrier-injection microring modulators can be found in [69] which includes both non-linear electrical and optical dynamics. Fig. 5(b) shows through port optical spectra from a 5 µm radius microring resonator with applied bias voltages of 0 V and 0.86 V [69]. Relying on the high modulation depths and efficient bias resonance wavelength response, the carrier-injection modulators of extremely high energy efficiency have been demonstrated in photonic interconnects [70]. However, their speed with simple non-return-to-zero (NRZ) modulation is limited by both long minority carrier lifetimes and series resistance effects.

In this context, pre-emphasis signaling that improves the optical transition time is necessary for achieving data rates up to 10 Gb/s with carrier-injection ring modulators [71]. As the effective device time constant is varying during a rising transition, where it is limited by long minority carrier lifetimes, versus a falling transition, where it is limited by series resistance, nonlinear pre-emphasis waveforms are often used. As shown in the experimental setup of Fig. 6(a), differential outputs from a high-speed pattern generator are combined to generate a pre-emphasis drive signal. The improvement is normally investigated by varying the pre-emphasis pulse duration, pulse depth, and DC bias, with a given swing (e.g., V_{pp} of 2 V). As predicted by the carrier-injection microring modulator model [69], utilizing a simple drive signal that is centered at a 0.7 V bias without pre-emphasis results in a completely closed eye diagram with a 2^7-1 data pattern (Fig. 6(b)). In comparison, as shown in Fig. 6(c), utilizing an optimal pre-emphasis driving signal with 0.8 V pulse depth, 0.7 V dc bias, and pulse duration of 80 ps allows to achieve a clear eye opening at 8 Gb/s.

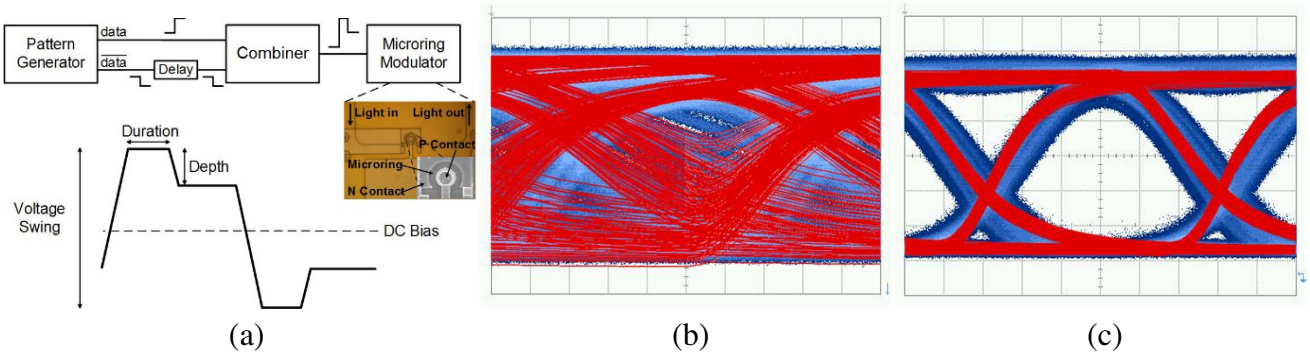

Figure 6. (a) Pre-emphasis NRZ signal generation and waveform; Impact of pre-emphasis on 8 Gb/s measured (blue) and simulated (red) optical eye diagrams: (b) no pre-emphasis; (c) with 0.8 V pulse depth, 0.7 V dc bias, and pulse duration of 80 ps [69].

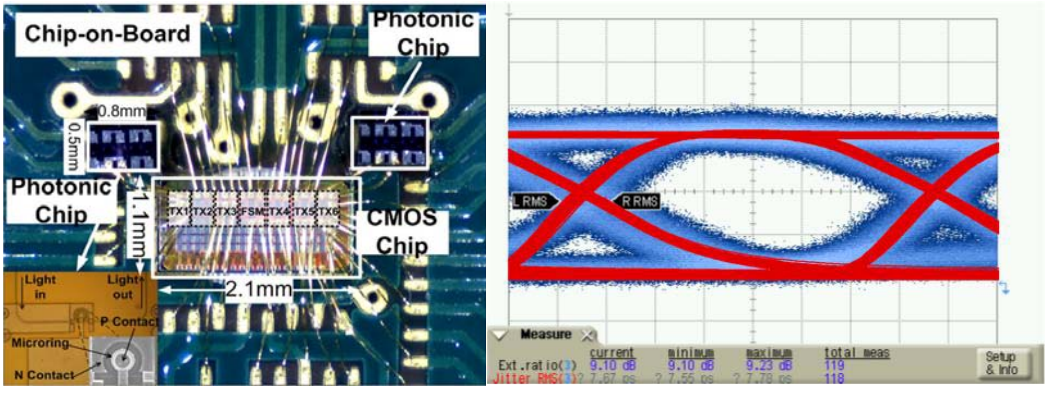

Figure 7. (a) Hybrid-integrated optical transmitter prototype with a 5 µm radius carrier-injection microring modulator and a 65 nm CMOS IC driver; (b) 9 Gb/s measured (blue) and co-simulated (red) optical eye diagrams with the microring resonator modulator driven by the 65 nm CMOS driver [69].

CMOS integrated circuits are promising to realize high energy efficiency links due to their low voltage supply and low power consumption. As shown in a hybrid-integrated prototype of carrier-injection microring resonator-based transmitter in Fig. 7(a), the pre-emphasis NRZ driver implemented in a 65 nm CMOS technology [71] is wire bonded both to the PCB and the silicon ring modulator for testing. While the pre-emphasis pulse depth is fixed in this CMOS driver implementation, the prototype has the ability to adjust the DC bias and the pre-emphasis pulse duration in an asymmetric manner for independent optimization of the rising and falling responses. Fig. 7(b) shows a measurement of an optimal modulation of 9 Gb/s where co-simulated eye diagrams (use the model in [69]) are achieved when the bias voltage is 1.45 V, with asymmetric pulse durations for rising and falling transitions of 70 ps and 50 ps, respectively. Unfortunately, high-speed silicon carrier-injection modulators have not been demonstrated with PAM4 signaling due to the device high nonlinearity.

3.2.2. Carrier-Depletion Microring Modulators

As shown on the left side of Fig. 8, the carrier-depletion microring modulator similarly consists of a ring resonator coupled to a straight waveguide, but with a PN junction in the waveguide center. This configuration, where the fast stretch of depletion region is achieved under reverse bias, allows shorter transferring distance and sequent faster carrier response. The overall data capacity of carrier-depletion modulators can be further scaled up by using PAM4 signaling, which is frequently used for simultaneously achieving longer transmission distances and operation with eased demand on the electro-optic bandwidth compared to NRZ modulation. A straightforward way to implement PAM4 modulation for microring modulators involves driving a single-segment device with different DAC-generated voltage levels. Alternatively, reduced transmitter complexity is possible by segmenting the modulator into two MSB (Most Significant Bit) and LSB (Least Significant Bit) phase shifters of different lengths that are driven by two simple NRZ drivers. As shown by the left structure of Fig. 8, a conventional ring resonator modulator utilizes a single PN junction phase shifter in the ring waveguide which is formed by outer p+ and inner n+ doping and additional p++ and n++ regions for ohmic contacts. Splitting this phase shifter into multiple segments allows multi-level modulation as shown by the right PAM4 structure which has longer MSB and shorter LSB segments.

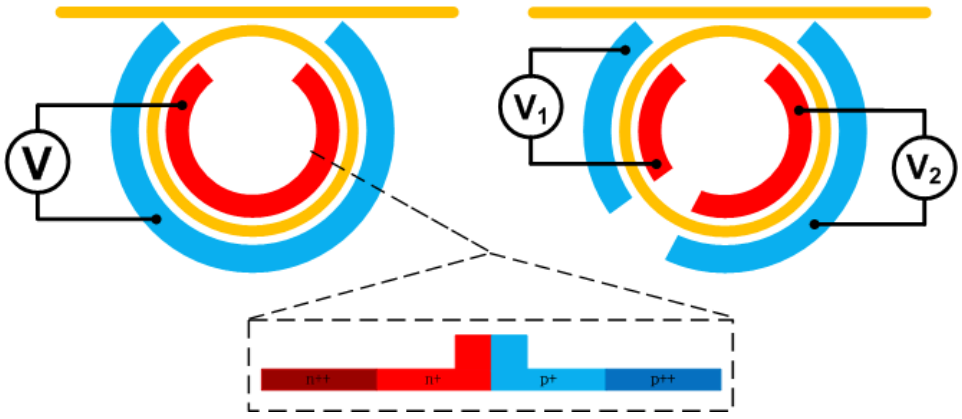

Figure 8. Top and cross section views of carrier-depletion microring modulators with (a) a single phase shifter segment and (b) segmented for PAM4 modulation with MSB and LSB phase shifters.

The transmission curves at four bias levels of a carrier-depletion microring modulator are shown in Fig. 9. A maximum V_{pp} swing of 4.4 V is used with consideration on the capacitive voltage division associated with the AC-coupling that maintains reverse-bias operation [72]. The total modulator nonlinearity resulted from the voltage-to-index and index-to-intensity responses has to be taken into account for forming identical PAM4 level spacing, with the input laser wavelength optimized separately for the single and two-segment devices. The overall nonlinearity is compensated in the two-segment design by adjusting the MSB:LSB length ratio to 1.9 : 1 from the ideal 2 : 1 ratio [73].

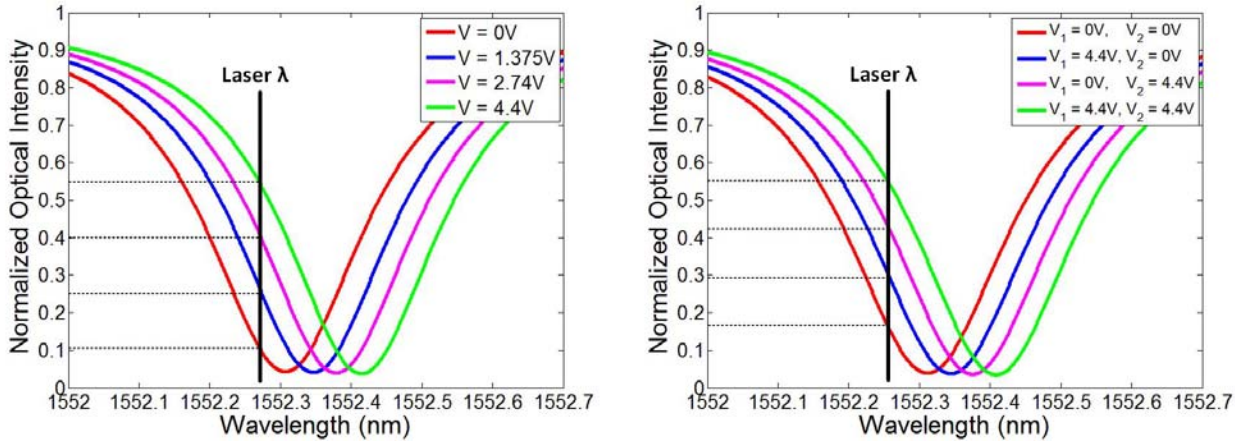

Figure 9. Optical transmission spectrum with PAM-4 signaling levels: (a) one-segment ring modulator and (b) two-segment ring modulator [73].

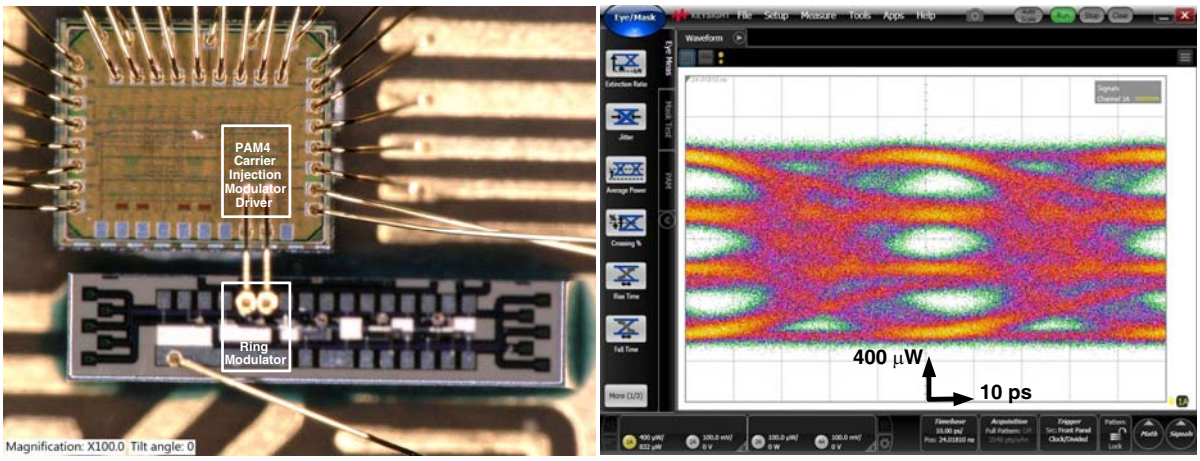

Figure 10. (a) Hybrid-integrated PAM4 transmitter prototype with a 7.5 μm radius single-segment carrier-depletion microring modulator and a 65 nm CMOS IC driver; (b) Measured optical eye diagrams at 40 Gb/s [74].

A microring modulator based PAM4 transmitter using an electrical digital-to-analog converter (DAC) has been demonstrated as shown in Fig. 10. This silicon microring modulator was fabricated in a 130 nm silicon-on-isolator (SOI) process [74]. Fig. 10(a) shows a hybrid-integrated PAM4 transmitter prototype with a 7.5 μm radius single-segment carrier-depletion microring modulator and a 65 nm CMOS IC driver [74], which is able to achieve 40 Gb/s PAM4 as shown in Fig. 10(b). A hybrid-integrated PAM4 transmitter prototype with a 10 μm radius two-segment carrier-depletion microring modulator and a 65 nm CMOS IC driver using an optical DAC is shown in Fig. 11(a) [75]. The 40 Gb/s PAM4 optical measurement results are depicted in the eye-diagrams of Fig. 11(b). Higher data rates can be achieved by adding pre-emphasis equalization to CMOS drivers.

The poor modulation efficiency of carrier-depletion microring modulators requires a large driving voltage as shown in Fig. 9, which can be improved by increasing the overlap of the PN junction and the optical mode. With further optimization on the PN junction profile (L shape) and the RC time constant, a 128 Gb/s PAM4 silicon photonic carrier-depletion microring modulator with 50 GHz electro-optic (EO)

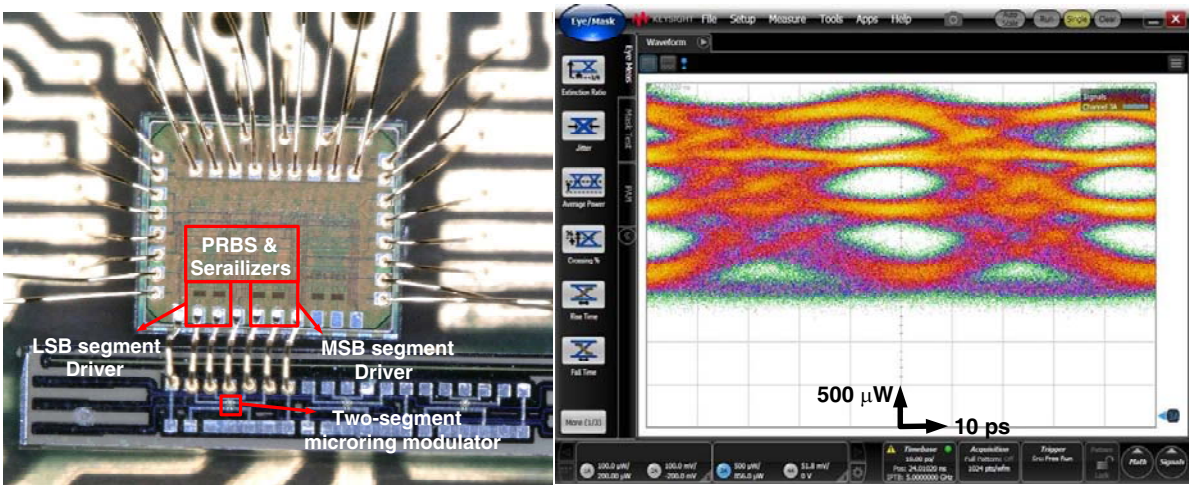

(a) (b)

Figure 11. (a) Hybrid-integrated PAM4 transmitter prototype with a 10 μm radius two-segment carrier-depletion microring modulator and a 65 nm CMOS IC driver; (b) Measured optical eye diagrams at 40 Gb/s [75].

bandwidth and 0.52 V·cm phase efficiency ($V_\pi L$) has been demonstrated recently [76]. In this case, a 2 V swing is able to provide sufficient modulation of the microring modulator, which indicates significant improvement in power consumption. A 112 Gb/s PAM4 transmitter with the silicon photonics microring modulator and a CMOS driver are also reported for 400G Ethernet applications [77].

3.2.3. Microring Modulator Based DWDM

As shown in Fig. 12, compact and energy efficient WDM interconnect architectures based on silicon microring resonator modulators and drop filters [78] are among the alternatives, as these high-Q devices occupy smaller footprints than large-area MZ modulators [79] and offer inherent wavelength multiplexing without extra device structures, such as array waveguide gratings (AWGs). As a request for WDM system, the multi-channel wavelengths from lasers, microring modulators, and microring filters have to be aligned to each other, which requires a feedback loop control circuits to stabilize resonant wavelengths in case high-Q cavity and the high thermo-optic coefficient strongly influence the working point. Numerous investigation have been conducted for improving the thermal efficiency of

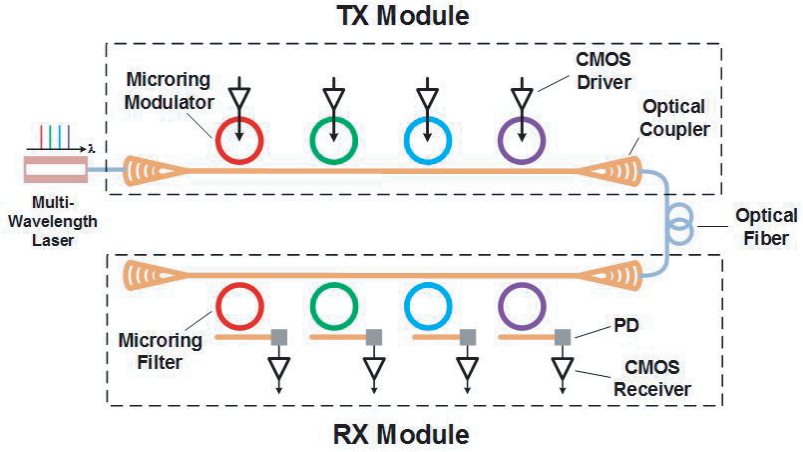

Figure 12. Silicon microring resonator-based WDM interconnect system.

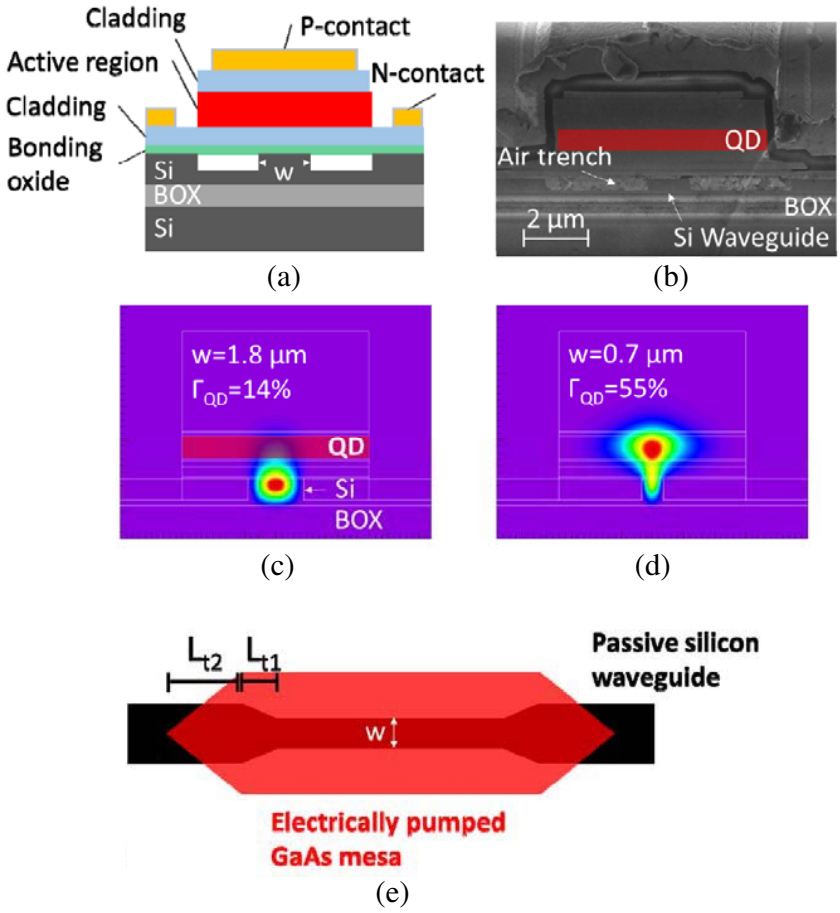

Figure 13. (a) Device cross-sectional diagram. (b) Scanning electron micrograph of a polished cross section. Fundamental mode calculation for (c) 1.8- and (d) 0.7-µm-wide silicon waveguide underneath a 6-µm-wide III-V mesa. (e) Schematic diagram of the taper design [85].

integrated heater in microring modulators and the adaptive wavelength stabilization circuits, in order to provide higher system robustness [72, 76].

The low cost and highly reliable light source is critical to develop silicon photonic integration, especially for achieving DWDM silicon photonic interconnects. Quantum dot (QD) comb lasers have many intrinsic benefits to be chosen as silicon on-chip laser sources. Due to the three dimensional confinement of carriers, QD lasers have higher temperature stability and lower threshold current densities when compared to conventional quantum well (QW) lasers [80]. QD lasers have a wider gain bandwidth than QW lasers due to the effect of inhomogeneous line broadening on gain [81], which is ideal for a DWDM link with a large amount of channels. It has also been found that QD lasers have a low relative intensity noise (RIN) [82] and less sensitivity to feedback [83], which reduces the requirements of isolators, thereby reducing the complexity and the cost of photonic transceivers. Using a comb laser instead of multiple single wavelength lasers such as DFB lasers reduces the complexity and the cost of link systems as well. More importantly, comb lasers have uniform channel spacing, which do not require to tune the wavelength of each channel individually. These advantages make QD comb lasers attractive as the laser source of DWDM silicon photonic links.

A hybrid QD comb laser on SOI substrate using an O_2 plasma-assisted direct bonding process [84] is shown in Fig. 13 [85]. Using a fixed mesa width and etch depth, lasers with varying confinement factors can be realized as the overlap of the optical mode with the QD region can be tuned by adjusting the width 'w' of the silicon waveguide, with no change in the III-V mesa width or etch depth. The optical mode can be transferred to and from the silicon waveguide using mode converters (tapers) in

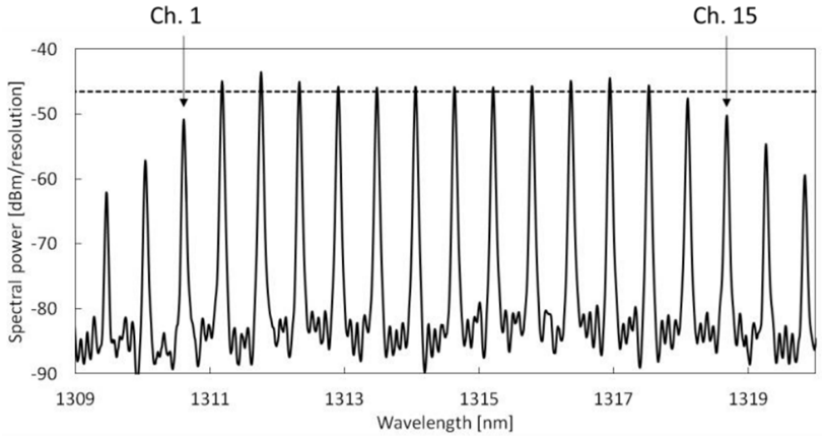

Figure 14. A QD comb laser optical spectrum where the dotted line is 3 dB below the highest power channel [86].

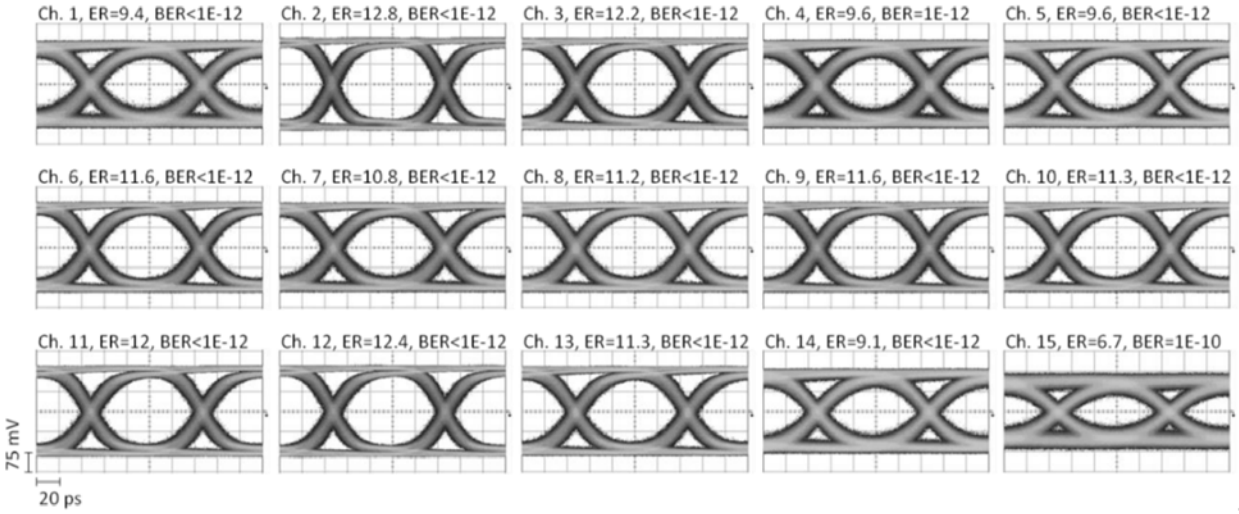

Figure 15. Eye diagrams of the 15 highest power channels with respective ER and BER values [86].

the silicon waveguide, thus relaxing the tolerance on the photolithographic alignment and resolution during the III-V mesa lithography and etch. The 15 highest power comb lines from the QD comb laser (Fig. 13) with a channel spacing of 102 GHz is shown in Fig. 14 [86]. Eye diagrams for the 15 channels at 10 Gb/s with extinction ratio (ER) of 9.6 or better are shown in Fig. 15. A bit error rate (BER) of 10^{-12} or better in 14 channels was observed. The channel spacing of the QD comb laser is wide enough to realize more than 100 Gb/sPAM4 signaling for each channel, allowing aggregated > 1 Tb/s microring modulator based photonic interconnects in potential.

3.3. Silicon Photonic Crystal Modulators

In addition to the microring resonator, photonic crystal (PhC) is also a promising approach to realize low-power-consumption on-chip modulators, as listed and compared in Table 2. The intrinsic nature of light-matter enhancement of Bloch mode in PhC enables the tremendous reduction in footprint and the driving demand, which has been witnessed in PhC Mach-Zehnder (MZ) modulators [87, 88]. MZ modulators using silicon rib waveguide and plasmonic dispersion effect are typically configured with a length in mm scale for a compromised balance of driving amplitude and sufficient phase difference. By integrating PhC with silicon MZ structures, the length of silicon MZ modulators can be shortened to no more than 200 μm without sacrifice on the driving voltage and the bandwidth [87, 88]. A magnified

Table 2. Performance comparison of silicon photonic crystal modulators.

Reference	Length (μm)	Data Rate (Gbps)	ER (dB)	IL (dB)	V_{pp} (V)	Energy consumption	Technology
[88]	200	25	7	5	3.5	2.91 pJ/bit	MZ modualtor
[89]	6	3	8	1	0.05	2 fJ/bit	1D-silicon photonic crystal
[90]	16	> 10	20	3	0.5	< 1 fJ/bit	Fanoresonances in 1D silicon nanobeam cavity

group index of 8–9 and a sequent $V_\pi L$ of 0.056 V/cm can be experimentally obtained, simultaneously with an optical bandwidth covering full C-band. Moreover, the size of the modulator can be further reduced by using the resonant counterparts, i.e., two-dimension/one-dimension (2D/1D) PhC cavities. Particularly, the 1D nanobeam PhC cavity is reasonably preferred as it shows the ability of further compressing the transverse dimension, while keeping a competent Q factor as 2D PhC cavity. This model is theoretically investigated and a high extinction ratio of 8 dB is predicted, with a tiny driving voltage of 0.05 V and an ultra-compact footprint of 6 μm [89]. However, as well known that modulation speed is simultaneously governed by the RC impedance and the photon lifetime, the excessive Q factor (e.g., few millions in [89]) which the high modulation efficiency benefits from has put a ceiling of 3 Gb/s in this configuration. This well happens in high-Q cavity where the flipping of output signal is mainly blocked by the temporally-long decay of optical mode in Lorentzian-shape. Giving a certain driving amplitude, the dominating challenge is how to balance this Q-Extinction trade-off (i.e., power consumption and speed trade-off). To go beyond this limitation, novel optical structures and novel schemes for carrier control are highly desired.

To make the required modulation speed of the resonant modulator feasible, in terms of the optical way, the Q factor has to be limited in a few thousands (for a modulation speed up to 30 GHz). To further increase the modulation efficiency and reduce the power consumption under such a condition, we may introduce Fano resonance. As we know, a Fano resonance arises from the interference between a discrete resonance and a continuum, which gives birth to the asymmetric resonant spectrum with an adequate mixture of them. This asymmetric spectrum allows more efficient on-off transition between maximum reflection and maximum transmission compared to the classical Lorentzian-type cavities (e.g., ring resonators) with similar quality factors. A Fano resonator can be practically and normally implemented in a planar photonic platform by placing a side-coupled bus waveguide (the "continuum") in the vicinity of a photonic cavity (the "discrete resonance"), whose coupling and decay rates are controlled by a small partially transmitting element (PTE). Instead of using these classical configurations, recently researchers have proposed to utilize a single nanobeam for achieving Fano resonance [90]. The device structure and

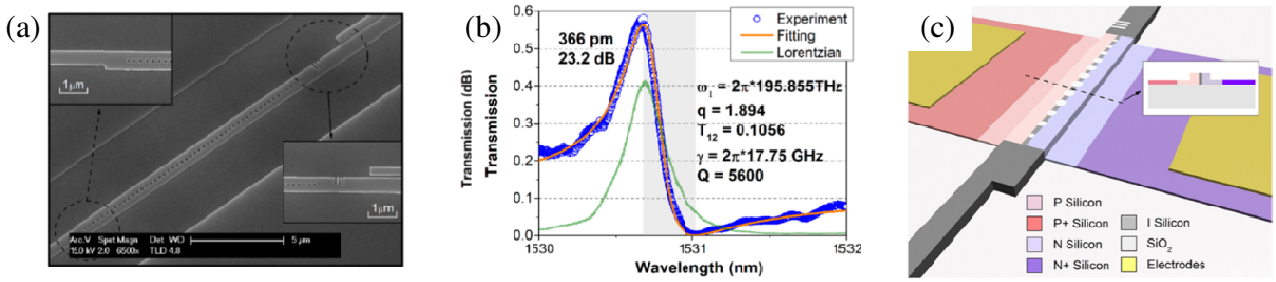

Figure 16. (a) SEM views of fabricated fano resonance PhC waveguide. (b) Experimental transmission and fitting curve of the second cavity mode of the nanobeam waveguide, depicted by blue circles and orange curves, respectively. (c) Proposed Fano modulator based on rib silicon PN depletion structure. Inset is the cross-section of the rib structure at the position labeled by the dotted line. Figures are reproduced from [90].

the spectrum of the Fano resonance are shown in Fig. 16. Compared to this classical configurations, the method proposed in [90] is to take the advantage of a two-mode spatial multiplexing scheme to generate the resonant and transmitting modes in the same physical optical waveguide, and consequently there is no demand on any waveguide-cavity coupling and no need for extended doped silicon area to avoid optical losses. An extinction ratio of 23 dB in a wavelength detuning of merely $\Delta\lambda = 366$ pm has been experimentally achieved with a Q factor of only 5600. While showing an intrinsically suitable structure for electro-optic resonant modulator, this configuration extremely compresses the active volume and the energy consumption for an extinction of 23 dB is theoretically reduced down to 1 fJ/bit, without sacrificing the modulation speed with a considerable Q factor.

4. HYBRID SILICON MODULATORS

In addition to the full silicon approaches, huge efforts have also been witnessed in developing silicon hybrid photonic devices, which target high modulation speed as well as compact device footprint, low insertion loss and as-low-as-possible driving voltage [91, 92]. These devices are demonstrated through different platforms, including hybrid organic-silicon modulators [93], hybrid graphene-silicon modulators [94], hybrid BTO silicon modulators [95], hybrid III-V silicon modulators [96], and hybrid $LiNbO_3$ silicon modulators [97] etc. Among these demonstrations, hybrid III-V/silicon or hybrid $LiNbO_3$/silicon modulators present outstanding performance, however, only modulators using bulk III-V and $LiNbO_3$ materials have been successfully used in commercial products since hybrid integration will introduce new instabilities which additionally raising the cost. Heterogeneous integration of III-V (or $LiNbO_3$) on silicon could be realized by benzocyclobuten (BCB) adhesive bonding process or O_2 plasma assisted direct bonding with a thin Al_2O_3 deposited layer before physical contact [98]. In this context, we will review some recent progresses in hybrid III-V and $LiNbO_3$ silicon modulators, which can also be characteristically categorized as electroabsorption modulators (EAMs) and electro-optic modulators (EOMs) according to the modulation mechanism.

4.1. Hybrid Electroabsorption Modulators

Hybrid III-V Silicon Modulators are basically achieved in electro-absorption type, which modifies the optical loss using quantum-confined stark effect (QCSE) or band filling effect [99]. EAMs show numerous merits in devices footprint, modulation speed, modulation efficiency as well as the flexibility of functional integration with laser sources. Duo-binary signal transmitters based on EAMs and DFBs on hybrid III-V/silicon platform have been demonstrated with a capacity over 100 Gb/s [100]. Intrinsically an EAM can also be used as a photodetector since light absorbed in III-V materials could be further converted into photocurrent. An on-chip transceiver demonstrated using hybrid III-V silicon EAMs are shown in Fig. 17 [101]. In this configuration, the EAM can be either used as a modulator or a photodetector, which strongly reduces the fabrication complexity. A six-channel wavelength-division-multiplexed on-chip optical transceiver was further achieved by integrating the EAMs with an arrayed waveguide grating (AWG) (de)multiplexer. To fully take advantages of the fast electro-absorption effect, the EAMs are driven through travelling wave electrode (TWE) instead of lump electrode. TWE is widely used to address the impedance mismatch induced reflection and velocity mismatch between electrical and optical signals, which were demonstrated with a bandwidth over 67 GHz in the early years [99]. The driving voltage of hybrid III-V silicon EAMs can be further reduced by introducing band-filling effect, e.g., a hybrid III-V silicon EAM driven with signal as low as 50 mV [102]. These four modulators are listed in Table 3 for comparison. Though electro-absorption modulators based on band filling effect require the lowest driving voltage swing, the electro-optic bandwidth is limited to no more than 2 GHz. Instead, hybrid III-V on silicon EAMs combining QCSE and TWE show no compromise on any figure of merits, which will be considered as an attractive candidate for 400 G Ethernet.

4.2. Hybrid Electro-Optic Modulators

Compared to EAMs, EOMs have larger optical bandwidth, higher modulation speed, and more modulation formats. The optical bandwidth of EAMs is typically less than 30 nm. However, EOMs can achieve 100 nm optical bandwidth. A hybrid III-V silicon MZ modulator with capacitively loaded

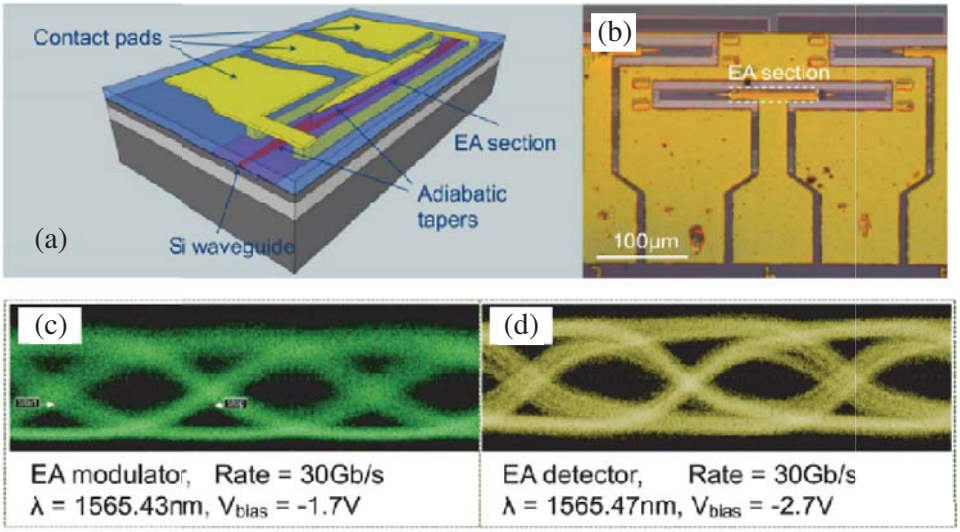

Figure 17. (a) Three-dimensional sketch of the III-V/Si hybrid integrated EA section. (b) Top view of one fabricated EA section. (c) 30 Gb/s eye pattern for modulation of a standalone EA device. (d) 30 Gb/s eye pattern for detection of a standalone EA device [101].

Table 3. Performance comparison of hybrid III-V on silicon electroabsorption modulators.

Reference	Length (μm)	Data Rate (Gb/s)	ER (dB)	IL (dB)	V_{pp} (V)	Technology
[100]	200	100	15	-	2.5	Hybrid III-V on silicon modulator integrated with laser
[101]	100	30	6.9	2	0.8	Hybrid III-V on silicon modulator integrated with detector
[99]	100	50	9.6	4.9	2.2	Hybrid III-V on silicon modulator with travelling wave electrode
[102]	80	1.25	6.3	5	0.05	Hybrid III-V on silicon modulator with band-filling effect

traveling wave electrode which reduces electrical propagation loss and increases device impedance has been demonstrated [103]. Using push-pull configuration, a data rate of 40 Gb/s and a voltage-length product of 0.24 V·cm were achieved. The modulator has low chirp due to the linear relationship between the phase changing and the applied voltage. Charging and discharging the metal-oxide-semiconductor (MOS) capacitor can cause plasma dispersion and modulation of the laser output power. Similar to previously demonstrated pure Si MOS modulators, this heterogeneous MOS capacitor is extremely useful to introduce the plasma dispersion effect [38] into the heterogeneous photonic device platform. EOMs using InGaAsP/Si hybrid MOS capacitors have been demonstrated [104, 105]. The optical mode has a large overlap with carriers in the n-InGaAsP/Al_2O_3/p-Si MOS capacitor that achieves a voltage-length product as low as 0.047 V·cm which has almost 5× smaller than a typical hybrid III-V silicon modulator. The bandwidth limit of hybrid MOS EOMs due to the lump electrode can be improved by adopting capacitively loaded traveling wave electrode.

The hybrid MOS structure can be implemented in microring modulators to further reduce the footprint and the voltage-length product. As shown in Fig. 18, a hybrid III-V silicon transmitter based on microring laser with thermal shunt, MOS capacitor and CMOS driver has been demonstrated [106, 107]. The thermal shunt is used to transfer the Joule heat directly to substrate by good thermal conductivity metals. The MOS capacitor is a new scheme to introduce electro-optic effect

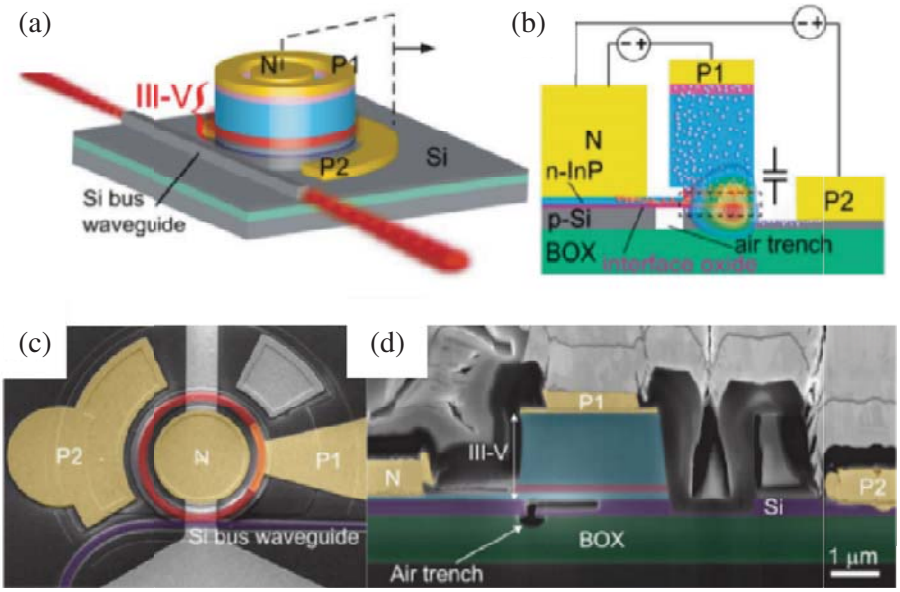

Figure 18. (a) Schematic of the heterogeneous laser with proposed three terminal laser structure. (b) Cross-sectional schematic of the three terminal heterogeneous microring laser with simulated fundamental lasing mode. SEM images of the fabricated laser from (c) top view and (d) cross-section [106].

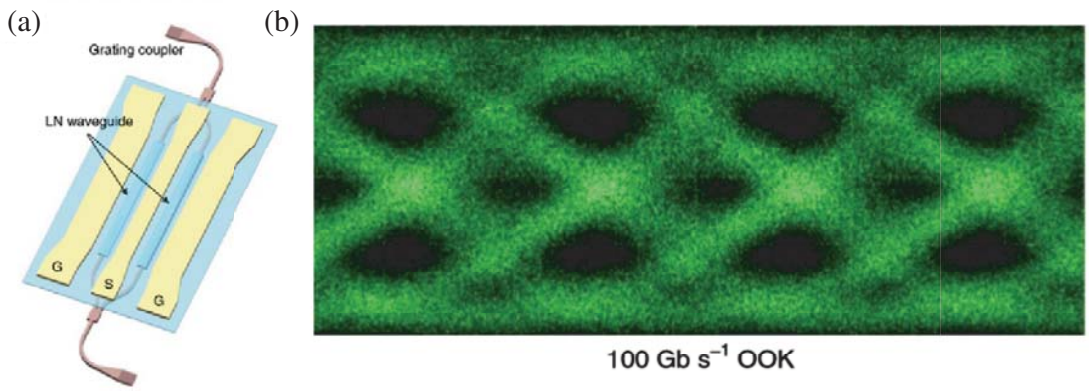

Figure 19. (a) Schematic of the hybrid lithium niobate silicon MZ modulator. (b) An optical eye diagram at 100 Gb/s with a 5 dB dynamic extinction ratio [97].

in laser cavity. The refractive index and free-carrier absorption loss in InP and Si materials change as a result of free carriers accumulating or depleting near the gate oxide under an external bias. Thus phase tuning or data modulation can be achieved. In order to realize a heterogeneous waveguide where the optical mode(s) overlap with the MOS capacitor, a "staircase" shape of the waveguide geometry is designed as shown in Fig. 17(b). It is similar to Si MOS-type waveguide based on the Poly-Si/gate oxide/crystalline Si structure [28] except that the Poly-Si layer is replaced by a layer of crystalline III-V material. A large variety of III-V compound semiconductor, primarily InP or GaAs based materials in our applications, can be flexibly chosen to form such a heterogeneous MOS capacitor. Due to much smaller conductivity electron effective mass and larger electron mobility in InP and GaAs than these of crystalline Si, plasma dispersion effect-induced index change in n-type InP and GaAs is much more effective and free carrier absorption is lower. However, similarity in those parameters for holes among them does not give advantages to III-V materials over Si, and the hole-induced intervalenceband absorption is much larger in InP and GaAs on the contrary. Coincidently, free holes can lead to larger

index change than electrons in Si. Therefore a heterogeneous capacitor with n-type III-V and p-type Si is a natural choice to maximize the carrier-induced index change.

Hybrid $LiNbO_3$ silicon modulators have also attracted due to their large modulation bandwidth thanks to the fast Pockels effect. A hybrid lithium niobate silicon MZ modulator with a data rate over 100 Gb/s has been demonstrated as shown in Fig. 19 [97]. The high-performance modulator is realized by seamless integration of a high-contrast waveguide based on lithium niobate with compact, low-loss silicon circuitry. The light is coupled between silicon waveguide and lithium niobate waveguide through a vertical adiabatic coupler. The insertion loss for a 5 mm device is only 2.5 dB due to the low intrinsic absorption in lithium niobate. In Table 4 we compare the four MZ electro-optic modulators based on hybrid silicon platform. As shown in Table 4, the hybrid $LiNbO_3$ on silicon modulator has the highest modulation speed but suffers largest $V_\pi L$. Hybrid III-V silicon modulators based on a MOS capacitor have stronger electro-optic effect than the $LiNbO_3$ modulator while the speed is limited by the electrical parasitics.

Table 4. Performance comparison of hybrid silicon electro-optic modulators.

Reference	Length (μm)	Data Rate (Gbps)	ER (dB)	IL (dB)	V_{pp} (V)	$V_\pi L$ (V·cm)	Technology
[103]	500	40	11	4.5	4	0.24	Hybrid III-V on silicon modulator
[104]	500	106	13.8	0.95	< 0.8	0.047	Hybrid III-V on silicon modulator
[105]	250	32	3.1	1.0	0.9	0.09	Hybrid III-V on silicon modulator
[97]	5000	100	5.0	2.5	4	2.2	Hybrid $LiNbO_3$ on silicon modulator

5. DISCUSSION

Table 5 lists performances of discussed modulators with more than 10 Gb/s data rates, including modulation efficiency ($V_\pi L$ or $V_{pp}L$), modulation bandwidth, insertion loss (IL) and energy efficiency (Joule/bit). One can see that silicon photonics MZ modulators and Hybrid $LiNbO_3$ on silicon MZ modulators have the lowest modulation efficiency due to the inefficient silicon plasma dispersion effect or weak $LiNbO_3$ Pockels effect. Silicon photonics modulators with high Q-factor using microring resonators or photonic crystal (PhC) show one or two order of magnitude higher modulation efficiency. In addition to use the high-Q resonance effect, hybrid III-V on silicon is another approach to enhance the modulation efficiency. As listed in Table 5, the modulation bandwidth of larger than 50 GHz can be achieved with silicon photonics PN modulators, hybrid III-V on silicon EAMs, or hybrid $LiNbO_3$ on silicon modulators. The modulation bandwidth of lump modulators (small footprint) with high-Q factor are mainly determined by both the electrical parasitics and the photon lifetime. The Q-factor of silicon microring or PhC modulators requires to be designed properly to balance the modulation efficiency and the bandwidth. Although traveling wave MZ modulators have no concerns of the photo lifetime, due to the large footprint, the modulation bandwidth may be limited by the mismatch of impedances and velocities between the electrode and the device. As listed in Table 5, modulators can be operated at much higher data rates than their bandwidths by implementing pre-emphasis equalization such as a finite impulse response (FIR) filter [70, 105]. Additionally, advanced modulation techniques such as PAM4 [76, 104] and duo-binary [100] are another alternative to increase the data rate.

As listed in Table 5, modulators with higher modulation efficiency, e.g., high-Q modulators and hybrid III-V on silicon modulators, usually own higher energy efficiency due to the smaller footprint or lower driving voltage. Typically, modulators with higher Q-factor result in higher energy efficiency, e.g., silicon carrier-injection microring modulators with $Q \sim 12000$ [70] obtain higher energy efficiency than carrier-depletion microring modulators with $Q \sim 5000$ [76]. It is worth noting that the calculated energy efficiency in Table 5 is the power consumed on the device only. As we mentioned, transmitter circuitry contributes quite large power consumption. A CMOS silicon carrier-injection microring modulator transmitter at a data rate of 9 Gb/s has achieved an energy efficiency of 473 fJ/bit [71] which is almost 100× worse than the energy efficiency of 5 fJ/bit counting the device only [70]. Similarly, a CMOS

Table 5. Performance comparison for different types of modulators.

Reference	Length (μm)	EO Bandwidth (GHz)	Data Rate (Gbps)	ER (dB)	IL (dB)	V_{pp} (V)	$V_\pi L$ (V·cm)	Energy Efficiency (fJ/bit)	Technology
[62]	750	> 38	60	4.4	2	6	1.8	3200	Silicon p-n MZ
[51]	3000	29	50	3.4	3.34	1.5	2.43	450	Silicon p-n MZ
[56]	750	27.8	50	7.5	6.5	6.5	2.05	1100	Silicon p-n MZ
[70]	10	1	12.5	10	0.2	0.9	0.03	5	Silicon p-i-n microring
[76]	20	50	128	6	3	2.4	0.52	65	Silicon p-n microring
[88]	200	-	25	7	5	3.5	< 0.06	2910	Silicon PhC MZ
[90]	16	-	> 10	20	3	0.5	-	< 1	Silicon PhC Fano resonance
[100]	200	20	100	15	-	2.5	-	-	Hybrid III-V on silicon (EAM)
[101]	100	13	30	6.9	2	0.8	-	-	Hybrid III-V on silicon (EAM)
[99]	100	> 67	50	9.6	4.9	2.2	-	608	Hybrid III-V on silicon (EAM)
[103]	500	27	40	11	4.5	4	0.24	2480	Hybrid III-V on silicon MZ (MOS)
[104]	500	-	106	13.8	0.95	< 0.8	0.047	< 44	Hybrid III-V on silicon MZ (MOS)
[105]	250	2.2	32	3.1	1.0	0.9	0.09	-	Hybrid III-V on silicon MZ (MOS)
[97]	5000	> 70	100	5.0	2.5	4	2.2	-	Hybrid $LiNbO_3$ on silicon MZ

silicon carrier-depletion microring modulator transmitter at a data rate of 112 Gb/s has achieved an energy efficiency of 6 pJ/bit [77] which is also around 100× worse than the energy efficiency of 65 fJ/bit counting the device only [76]. Therefore, reducing the power consumption from electronics is also crucial to improve the total energy efficiency. Certainly, a modulator with higher modulation efficiency requires lower driving voltage which saves the total power consumption of an optical transmitter [71, 77].

The device insertion loss is also an important metric for calculating the energy efficiency of a full optical link. Modulators with low insertion loss are always preferred because it can not only reduce the laser power consumption but also relieve the link budget requirement. As listed in Table 5, silicon carrier-injection modulators have extremely low insertion loss. However, their low bandwidth limits the applications in high-speed optical links. Overall, there are tradeoffs among the four metrics for different modulator categories. The optimum modulator may be different for various applications, depending on requirements of the bandwidth per channel and in total, the energy efficiency, the link budget, etc.

6. CONCLUSION

The main traffic of the global data communication occurs in data centers. Mega-data centers are emerging to relax the explosive Datacom growth. Multimode VCSEL interconnects are most commonly used in HPC and data centers due to their simplicity, low cost, and energy efficiency. However, it is a challenge to scale the bandwidth and the link distance to satisfy requirements for mega-data centers. External modulation techniques become more attractive than direct modulation due to the higher bandwidth and longer transmission distance. Silicon photonics interconnects are emerging to be widely used in mega-data centers thanks to their high bandwidth, low cost, and high integratability. Silicon photonics MZ modulators have been commercialized due to the high reliability and the insensitivity to temperature and wavelength. The modulation efficiency can be maximized by optimizing the doping profile, the overlap of the carrier change and the optical mode, and the electrode. However, the weak electro-optic effect in silicon limits the modulation efficiency and thereby the energy efficiency. High-Q resonant cavities can be used to enhance the EO effect which silicon photonics microring modulators with 10× better modulation efficiency are achieved. The natural wavelength multiplexing feature of

microring modulators are ideal for DWDM application assisted with frequency comb lasers. The slow-wave effect of silicon photonics crystal can also be implemented to enhance the modulation efficiency. Particularly, two or more effects or techniques can be combined together to enhance the modulation efficiency such as Fano resonance PhC cavity modulators. Hybrid silicon modulators are proposed to benefit from the low cost and high integration silicon platform as well as obtain better modulation performance by using heterogeneous integration. It allows to explore new materials to be integrated onto silicon to realize better performance. III-V on silicon modulators including EAMs and EOMs are preferred due to the high reliability, low loss, and high modulation efficiency.

ACKNOWLEDGMENT

The authors are grateful to the partial support of the National Key Research and Development Program of China (No. 2017YFA0205700), National Natural Science Foundation of China (NSFC) (11621101), and AOARD.

REFERENCES

1. Amann, M.-C. and W. Hofmann, "InP-based long-wavelength VCSELs and VCSEL arrays," *IEEE Journal of Selected Topics in Quantum Electronics*, Vol. 15, No. 3, 861–868, 2009.
2. Naoe, K., "High speed InP lasers for 400 GbE," *Proc. European Conference on Optical Communication (ECOC)*, Th1D.1, 2019.
3. Thomson, D., A. Zilkie, J. E. Bowers, T. Komljenovic, G. T. Reed, L. Vivien, D. Marris-Morini, E. Cassan, L. Virot, J.-M. Fédéli, J.-M. Hartmann, J. H. Schmid, D.-X. Xu, F. Boeuf, P. O'Brien, G. Z. Mashanovich, and M. Nedeljkovic, "Roadmap on silicon photonics," *Journal of Optics*, Vol. 18, No. 7, 073003, 2016.
4. Komljenovic, T., D. Huang, P. Pintus, M. A. Tran, M. L. Davenport, and J. E. Bowers, "Photonic integrated circuits using heterogeneous integration on silicon," *Proceedings of the IEEE*, Vol. 106, No. 12, 2246–2257, 2018.
5. Samani, A., M. Chagnon, D. Patel, V. Veerasubramanian, S. Ghosh, M. Osman, Q. Zhong, and D. V. Plant, "A low-voltage 35-GHz silicon photonic modulator-enabled 112-Gb/s transmission system," *IEEE Photonics Journal*, Vol. 7, No. 3, 7901413, 2015.
6. Manipatruni, S., K. Preston, L. Chen, and M. Lipson, "Ultra-low voltage, ultra-small mode volume silicon microring modulator," *Optics Express*, Vol. 18, No. 17, 18235–18242, 2010.
7. Nguyen, H. C., S. Hashimoto, M. Shinkawa, and T. Baba, "Compact and fast photonic crystal silicon optical modulators," *Optics Express*, Vol. 20, No. 20, 22465–22474, 2012.
8. Melikyan, A., L. Alloatti, A. Muslija, D. Hillerkuss, P. C. Schindler, J. Li, R. Palmer, D. Korn, S. Muehlbrandt, D. van Thourhout, B. Chen, R. Dinu, M. Sommer, C. Koos, M. Kohl, W. Freude, and J. Leuthold, "High-speed plasmonic phase modulators," *Nature Photonics*, Vol. 8, 229–233, 2014.
9. Kuo, Y.-H., Y. K. Lee, Y. Ge, S. Ren, J. E. Roth, T. I. Kamins, D. A. B. Miller, and J. S. Harris, "Strong quantum-confined Stark effect in germanium quantum-well structures on silicon," *Nature*, Vol. 437, 1334–1336, 2005.
10. Wang, C., M. Zhang, X. Chen, M. Bertrand, A. Shams-Ansari, S. Chandrasekhar, P. Winzer, and M. Lončar, "Integrated lithium niobate electro-optic modulators operating at CMOS-compatible voltages," *Nature*, Vol. 562, 101–104, 2018.
11. Schow, C. L. and K. Schmidtke, "INTREPID: Developing power efficient analog coherent interconnects to transform data center networks," *Optical Fiber Communications Conference and Exhibition (OFC)*, M4D.9, 2019.
12. Kerrebrouck, J. V., X. Pang, O. Ozolins, R. Lin, A. Udalcovs, L. Zhang, H. Li, S. Spiga, M.-C. Amann, L. Gan, M. Tang, S. Fu, R. Schatz, G. Jacobsen, S. Popov, D. Liu, W. Tong, G. Torfs, J. Bauwelinck, J. Chen, and X. Yin, "High-speed PAM4-based optical SDM interconnects

with directly modulated long-wavelength VCSEL," *IEEE/OSA Journal of Lightwave Technology*, Vol. 37, No. 2, 356–362, 2019.

13. Huynh, T. N., et al., "4×50 Gb/s NRZ shortwave-wavelength division multiplexing VCSEL link over 50 m multimode fiber" *Optical Fiber Communications Conference and Exhibition (OFC)*, Tu2B.5, 2017.
14. Lin, C.-K., A. Tandon, K. Djordjev, S. W. Corzine, and M. R. T. Tan, "High-speed 985 nm bottom-emitting VCSEL arrays for chip-to-chip parallel optical interconnects," *IEEE Journal of Selected Topics in Quantum Electronics*, Vol. 13, 1332–1339, 2007.
15. Tan, M. R. T., P. Rosenberg, W. V. Sorin, B. Wang, S. Mathai, G. Panotopoulos, and G. Rankin, "Universal photonic interconnect for data centers," *IEEE/OSA Journal of Lightwave Technology*, Vol. 36, 175–180, 2018.
16. Hatakeyama, H., T. Anan, T. Akagawa, K. Fukatsu, N. Suzuki, K. Tokutome, and M. Tsuj, "Highly reliable high-speed 1.1-μm-range VCSELs with InGaAs/GaAsP-MQWs," *IEEE Journal of Quantum Electronics*, Vol. 46, 890–897, 2010.
17. Lavrencik, J., S. Varughese, V. A. Thomas, G. Landry, Y. Sun, R. Shubochkin, K. Balemarthy, J. Tatum, and S. E. Ralph, "4λ × 100 Gbps VCSEL PAM-4 transmission over 105 m of wide band multimode fiber," *Optical Fiber Communications Conference and Exhibition (OFC)*, Tu2B.5, 2017.
18. Ralph, S. E. and J. Lavrencik, "High capacity VCSEL links," *Optical Fiber Communications Conference and Exhibition (OFC)*, Tu3A.1, 2019.
19. Horst, F., W. M. J. Green, S. Assefa, S. M. Shank, Y. A. Vlasov, and B. J. Offrein, "Cascaded Mach-Zehnder wavelength filters in silicon photonics for low loss and flat pass-band WDM (de-) multiplexing" *Optics Express*, Vol. 21, 11652–11658, 2013.
20. Dai, D., J. Wang, S. Chen, S. Wang, and S. He, "Monolithically integrated 64-channel silicon hybrid demultiplexer enabling simultaneous wavelength- and mode-division-multiplexing," *Laser Photonics Review*, Vol. 9, 339–344, 2015.
21. Pathak, S., P. Dumon, D. van Thourhout, and W. Bogaerts, "Comparison of AWGs and echelle gratings for wavelength division multiplexing on silicon-on-insulator," *IEEE Photonics Journal*, Vol. 6, 1–9, 2014.
22. Simpanen, E., J. S. Gustavsson, A. Larsson, M. Karlsson, W. V. Sorin, S. Mathai, M. R. Tan, and S. R. Bickham, "1060 nm single-mode VCSEL and single-mode fiber links for long-reach optical interconnects," *IEEE/OSA Journal of Lightwave Technology*, Vol. 37, 2963–2969, 2019.
23. Tan, M. R. T., B. Wang, W. V. Sorin, S. Mathai, and P. Rosenberg, "50 Gb/s PAM4 modulated 1065 nm single-mode VCSELs using SMF-28 for mega-data centers," *IEEE Photonics Technology Letters*, Vol. 29, 1128–1131, 2017.
24. Karinou, F., N. Stojanovic, A. Daly, C. Neumeyr, and M. Ortsiefer, "1.55-μm long-wavelength VCSEL-based optical interconnects for short-reach networks," *IEEE/OSA Journal of Lightwave Technology*, Vol. 34, 2897–2904, 2016.
25. Malacarne, A., F. Falconi, C. Neumeyr, W. Soenen, C. Porzi, T. Aalto, J. Rosskopf., M. Chiesa, J. Bauwelinck, and A. Bogon, "Low-power 1.3-μm VCSEL transmitter for data center interconnects and beyond," *Proc. European Conference on Optical Communication (ECOC)*, M.2.C.5, 2017.
26. Kapon, E. and A. Sirbu, "Long-wavelength VCSELs: Power-efficient answer," *Nature Photonics*, Vol. 3, 27–29, 2009.
27. Tansu, N., N. J. Kirsch, and L. J. Mawst, "Low-threshold-current-density 1300-nm dilute-nitride quantum well lasers," *Applied Physics Letters*, Vol. 81, No. 14, 2523, 2002.
28. Liu, A., R. Jones, L. Liao, D. Samara-Rubio, D. Rubin, O. Cohen, R. Nicolaescu, and M. Paniccia, "A high-speed silicon optical modulator based on a metal-oxide-semiconductor capacitor," *Nature*, Vol. 427, 615–618, 2004.
29. Sun, C., et al., "Single-chip microprocessor that communicates directly using light," *Nature*, Vol. 528, 534–538, 2015.
30. Atabaki, A. H., et al., "Integrating photonics with silicon nanoelectronics for the next generation of systems on a chip," *Nature*, Vol. 556, 349–354, 2018.

31. Idjadi, M. H. and F. Aflatouni, "Integrated Pound-Drever-Hall laser stabilization system in silicon," *Nature Communications*, Vol. 8, 1209, 2017.
32. El-Fiky, E., A. Samani, M. S. Alam, M. Sowailem, O. Carpentier, M. Jacques, L. Guenin, D. Patel, and D. V. Plant, "A 4-lane 400 Gb/s silicon photonic transceiver for intra-datacenter optical interconnects," *Optical Fiber Communications Conference and Exhibition (OFC)*, Th3A.3, 2019.
33. Shi, T., T. Su, N. Zhang, C. Hong, and D. Pan, "Silicon photonics platform for 400G data center applications," *Optical Fiber Communications Conference and Exhibition (OFC)*, M3F.4, 2018.
34. Nagarajan, R., M. Filer, Y. Fu, M. Kato, T. Rope, and J. Stewart, "Silicon photonics-based 100 Gbit/s, PAM4, DWDM data center interconnects," *Journal of Optical Communications and Networking*, Vol. 10, No. 7, B25–B36, 2018.
35. Harris, N. C., Y. Ma, J. Mower, T. Baehr-Jones, D. Englund, M. Hochberg, and C. Galland, "Efficient, compact and low loss thermo-optic phase shifter in silicon," *Optics Express*, Vol. 22, No. 9, 10487–10493, 2014.
36. Doylend, J. K., M. J. R. Heck, J. T. Bovington, J. D. Peters, L. A. Coldren, and J. E. Bowers, "Two-dimensional free-space beam steering with an optical phased array on silicon-on-insulator," *Optics Express*, Vol. 19, No. 22, 21595–21604, 2011.
37. Soref, R. and B. Bennett, "Electrooptical effects in silicon," *IEEE Journal of Quantum Electronics*, Vol. 23, 123–129, 1987.
38. Reed, G. T., G. Mashanovich, F. Y. Gardes, and D. J. Thomson, "Silicon optical modulators," *Nature Photonics*, Vol. 4, 518–526, 2010.
39. Debnath, K., D. J. Thomson, W. Zhang, A. Z. Khokhar, C. Littlejohns, J. Byers, L. Mastronardi, M. K. Husain, K. Ibukuro, F. Y. Gardes, G. T. Reed, and S. Saito, "All-silicon carrier accumulation modulator based on a lateral metal-oxide-semiconductor capacitor," *Photonics Research*, Vol. 6, 373–379, 2018.
40. Webster, M., C. Appel, P. Gothoskar, S. Sunder, B. Dama, and K. Shastri, "Silicon photonic modulator based on a MOS-capacitor and a CMOS driver," *IEEE Compound Semiconductor Integrated Circuit Symposium (CSICS)*, 2014.
41. Milivojevic, B., S. Wiese, J. Whiteaway, C. Raabe, A. Shastri, M. Webster, P. Metz, S. Sunder, B. Chattin, S. P. Anderson, B. Dama, and K. Shastri, "Silicon high speed modulator for advanced modulation: Device structures and exemplary modulator performance," *Proc. Silicon Photonics IX*, Vol. 8990, 899013, 2014.
42. Titriku, A., C. Li, A. Shafik, and S. Palermo, "Efficiency modeling of tuning techniques for silicon carrier injection ring resonators," *IEEE Optical Interconnects Conference (OI)*, 13–14, 2014.
43. Chen, C. H., C. Li, A. Shafik, M. Fiorentino, P. Chiang, S. Palermo, and R. Beausoleil, "A WDM silicon photonic transmitter based on carrier-injection microring modulators," *IEEE Optical Interconnects Conference (OI)*, 121–122, 2014.
44. Xu, Q., S. Manipatruni, B. Schmidt, J. Shakya, and M. Lipson, "12.5 Gbit/s carrier-injection-based silicon micro-ring silicon modulators," *Optics Express*, Vol. 15, 430–436, 2007.
45. Li, M., L. Wang, X. Li, X. Xiao, and S. Yu, "Silicon intensity Mach-Zehnder modulator for single lane 100 Gb/s applications," *Photonics Research*, Vol. 6, No. 2, 109–116, 2018.
46. Miller, D. A. B., "Energy consumption in optical modulators for interconnects," *Optics Express*, Vol. 20, No. 102, 293–308, 2012.
47. Liu, A., L. Liao, D. Rubin, H. Nguyen, B. Ciftcioglu, Y. Chetrit, N. Izhaky, and M. Paniccia, "High-speed optical modulation based on carrier depletion in a silicon waveguide," *Optics Express*, Vol. 15, No. 2, 660–668, 2007.
48. Sharif Azadeh, S., S. Romero-García, F. Merget, A. Moscoso-Mártir, N. von den Driesch, D. Buca, and J. Witzens, "Epitaxially grown vertical junction phase shifters for improved modulation efficiency in silicon depletion-type modulators," *Proc. SPIE Integrated Optics: Physics and Simulations II*, Vol. 9516, 95160T, May 2015.
49. Azadeh, S. S., F. Merget, S. Romero-García, A. Moscoso-Mártir, N. von den Driesch, J. Müller, S. Mantl, D. Buca, and J. Witzens, "Low V_π silicon photonics modulators with highly linear

epitaxially grown phase shifters," *Optics Express*, Vol. 23, No. 18, 23526–23550, 2015.

50. Dong, P., L. Chen, and Y.-K. Chen, "High-speed low-voltage single-drive push-pull silicon Mach-Zehnder modulators," *Optics Express*, Vol. 20, No. 6, 6163–6169, 2012.
51. Streshinsky, M., R. Ding, Y. Liu, et al., "Low power 50 Gb/s silicon traveling wave Mach-Zehnder modulator near 1300 nm," *Optics Express*, Vol. 21, No. 25, 30350–30357, 2013.
52. Li, Z.-Y., D.-X. Xu, W. R. McKinnon, S. Janz, J. H. Schmid, P. Cheben, and J.-Z. Yu, "Silicon waveguide modulator based on carrier depletion in periodically interleaved PN junctions," *Optics Express*, Vol. 17, No. 18, 15947–15958, 2009.
53. Xiao, X., H. Xu, X. Li, Y. Hu, K. Xiong, Z. Li, T. Chu, Y. Yu, and J. Yu, "25 Gbit/s silicon microring modulator based on misalignment-tolerant interleaved PN junctions," *Optics Express*, Vol. 20, 2507–2515, 2012.
54. Rosenberg, J. C., W. M. Green, S. Assefa, D. M. Gill, T. Barwicz, M. Yang, S. M. Shank, and Y. A. Vlasov, "A 25 Gbps silicon microring modulator based on an interleaved junction," *Optics Express*, Vol. 20, 26411–26423, 2012.
55. Thomson, D. J., F. Y. Gardes, J.-M. Fedeli, S. Zlatanovic, Y. Hu, B. P. P. Kuo, E. Myslivets, N. Alic, S. Radic, G. Z. Mashanovich, and G. T. Reed, "50-Gb/s silicon optical modulator," *IEEE Photonics Technology Letters*, Vol. 24, No. 4, 234–236, 2012.
56. Xiao, X., H. Xu, X. Li, Z. Li, T. Chu, Y. Yu, and J. Yu, "High-speed, low-loss silicon Mach-Zehnder modulators with doping optimization," *Optics Express*, Vol. 21, No. 4, 4116–4125, 2013.
57. Ziebell, M., D. Marris-Morini, G. Rasigade, J.-M. Fédéli, P. Crozat, E. Cassan, D. Bouville, and L. Vivien, "40 Gbit/s low-loss silicon optical modulator based on a pipin diode," *Optics Express*, Vol. 20, No. 10, 10591–10596, 2012.
58. Tu, X., T.-Y. Liow, J. Song, X. Luo, Q. Fang, M. Yu, and G.-Q. Lo, "50 Gb/s silicon optical modulator with traveling-wave electrodes," *Optics Express*, Vol. 21, No. 10, 12776–12782, 2013.
59. Gardes, F. Y., D. J. Thomson, N. G. Emerson, and G. T. Reed, "40 Gb/s silicon photonics modulator for TE and TM polarisations," *Optics Express*, Vol. 19, No. 12, 11804–11814, 2011.
60. Yong, Z., W. D. Sacher, Y. Huang, J. C. Mikkelsen, Y. Yang, X. Luo, P. Dumais, D. Goodwill, H. Bahrami, P. G.-Q. Lo, E. Bernier, and J. K. S. Poon, "U-shaped PN junctions for efficient silicon Mach-Zehnder and microring modulators in the O-band," *Optics Express*, Vol. 25, No. 7, 8425–8439, 2017.
61. Gardes, F. Y., A. Brimont, P. Sanchis, G. Rasigade, D. Marris-Morini, L. O'Faolain, F. Dong, J. M. Fedeli, P. Dumon, L. Vivien, T. F. Krauss, G. T. Reed, and J. Martí, "High-speed modulation of a compact silicon ring resonator based on a reverse-biased PN diode," *Optics Express*, Vol. 17, No. 24, 21986–21991, 2009.
62. Xiao, X., H. Xu, X. Li, Z. Li, T. Chu, J. Yu, and Y. Yu, "60 Gbit/s silicon modulators with enhanced electro-optical efficiency," *Optical Fiber Communications Conference and Exhibition (OFC)*, W4J.3, 2013.
63. Yang, Y., Q. Fang, M. Yu, X. Tu, R. Rusli, and G.-Q. Lo, "High-efficiency Si optical modulator using Cu travelling-wave electrode," *Optics Express*, Vol. 22, 29978–29985, 2014.
64. Xu, H., X. Xiao, X. Li, Y. Hu, Z. Li, T. Chu, Y. Yu, and J. Yu, "High speed silicon Mach-Zehnder modulator based on interleaved PN junctions," *Optics Express*, Vol. 20, 15093–15099, 2012.
65. Pantouvaki, M., P. Verheyen, J. De Coster, G. Lepage, P. Absil, and J. van Campenhout, "56 Gb/s ring modulator on a 300 mm silicon photonics platform," *European Conference on Optical Communication (ECOC)*, 2015.
66. Pitris, S., M. Moralis-Pegios, T. Alexoudi, Y. Ban, P. de Heyn, J. van Campenhout, and N. Pleros, "A 4×40 Gb/s O-band WDM silicon photonic transmitter based on micro-ring modulators," *Optical Fiber Communications Conference and Exhibition (OFC)*, W3E.2, 2019.
67. Dubé-Demers, R., S. LaRochelle, and W. Shi, "Ultrafast pulse-amplitude modulation with a femtojoule silicon photonic modulator," *Optica*, Vol. 3, No. 6, 622–627, 2016.
68. Liu, K., C. R. Ye, S. Khan, and V. J. Sorger, "Review and perspective on ultrafast wavelength-size electro-optic modulators," *Lasers & Photonics Reviews*, Vol. 9, No. 2, 172–194, 2015.

69. Wang, B., C. Li, C.-H. Chen, K. Yu, M. Fiorentino, R. G. Beausoleil, and S. Palermo, "A compact Verilog-A model of silicon carrier-injection ring modulators for optical interconnect transceiver circuit design," *IEEE/OSA Journal of Lightwave Technology*, Vol. 34, 2996–3005, 2016.
70. Chen, C. H., C. Li, A. Shafik, M. Fiorentino, P. Chiang, S. Palermo, and R. Beausoleil, "A WDM silicon photonic transmitter based on carrier-injection microring modulators," *IEEE Optical Interconnects Conference (OI)*, 121–122, 2014.
71. Li, C., R. Bai, A. Shafik, E. Z. Tabasy, B. Wang, G. Tang, C. Ma, C. H. Chen, Z. Peng, M. Fiorentino, R. G. Beausoleil, P. Chiang, and S. Palermo, "Silicon photonic transceiver circuits with microring resonator bias-based wavelength stabilization in 65 nm CMOS," *IEEE Journal of Solid-State Circuits*, Vol. 49, 1419–1436, 2014.
72. Li, H., Z. Xuan, A. Titriku, C. Li, K. Yu, B. Wang, A. Shafik, N. Qi, Y. Liu, R. Ding, T. Baehr-Jones, M. Fiorentino, M. Hochberg, S. Palermo, and P. Y. Chiang, "A 25 Gb/s, 4.4 V-Swing, AC-coupled ring modulator-based WDM transmitter with wavelength stabilization in 65 nm CMOS," *IEEE Journal of Solid State Circuits*, Vol. 50, 3145–3159, 2015.
73. Wang, B., K. Yu, H. Li, P. Y. Chiang, and S. Palermo, "Energy efficiency comparisons of NRZ and PAM4 modulation for ring-resonator-based silicon photonic links," *IEEE International Midwest Symposium on Circuits and Systems*, 2015.
74. Roshan-Zamir, A., B. Wang, S. Telaprolu, K. Yu, C. Li, M. A. Seyedi, M. Fiorentino, R. Beausoleil, and S. Palermo, "A 40 Gb/s PAM4 silicon microring resonator modulator transmitter in 65 nm CMOS," *IEEE Optical Interconnects Conference (OI)*, 8–9, 2016.
75. Roshan-Zamir, A., B. Wang, S. Telaprolu, K. Yu, C. Li, M. A. Seyedi, M. Fiorentino, R. Beausoleil, and S. Palermo, "A two-segment optical DAC 40 Gbps PAM4 silicon microring resonator modulator transmitter," *IEEE Optical Interconnects Conference (OI)*, 5–6, 2017.
76. Sun, J., M. Sakib, J. Driscoll, R. Kumar, H. Jayatilleka, Y. Chetrit, and H. Rong, "A 128 Gb/s PAM4 silicon microring modulator," *Optical Fiber Communications Conference and Exhibition (OFC)*, Th4A.7, 2018.
77. Li, H., G. Balamurugan, M. Sakib, J. Sun, J. Driscoll, R. Kumar, H. Jayatilleka, H. Rong, J. Jaussi, and B. Casper, "A 112 Gb/s PAM4 transmitter with silicon photonics microring modulator and CMOS driver," *Optical Fiber Communications Conference and Exhibition (OFC)*, Th4A.7, 2019.
78. Xu, Q., B. Schmidt, S. Pradhan, and M. Lipson, "Micrometre-scale silicon electro-optic modulator," *Nature*, Vol. 435, 325–327, 2005.
79. Liu, A., R. Jones, L. Liao, D. Samara-Rubio, D. Rubin, O. Cohen, R. Nico-laescu, and M. Paniccia, "A high-speed silicon optical modulator based on a metal-oxide-semiconductor capacitor," *Nature*, Vol. 427, 615–618, 2004.
80. Sugawara, M. and M. Usami, "Quantum dot devices handling the heat," *Nature Photonics*, Vol. 3, 30–31, 2009.
81. Ortner, G., C. N. Allen, C. Dion, P. Barrios, D. Poitras, D. Dalacu, G. Pakulski, J. Lapointe, P. J. Poole, W. Render, and S. Raymond, "External cavity InAs/InP quantum dot laser with a tuning range of 166 nm," *Apply Physics Letters*, Vol. 88, 121119, 2006.
82. Capua, A., L. Rozenfeld, V. Mikhelashvili, G. Eisenstein, M. Kuntz, M. Laemmlin, and D. Bimberg, "Direct correlation between a highly damped modulation response and ultra low relative intensity noise in an InAs/GaAs quantum dot laser," *Optics Express*, Vol. 15, 5388–5393, 2007.
83. Azouigui, S., D.-Y. Cong, A. Martinez, K. Merghem, Q. Zou, J.-G. Provost, B. Dagens, M. Fischer, F. Gerschutz, J. Koeth, I. Krestnikov, A. Kovsh, and A. Ramdane, "Temperature dependence of dynamic properties and tolerance to optical feedback of high-speed 1.3-µm DFB quantum-dot lasers," *IEEE Photonics Technology Letters*, Vol. 23, 582–584, 2011.
84. Liang, D. and J. E. Bowers, "Highly efficient vertical outgassing channels for low-temperature InP-to-silicon direct wafer bonding on the silicon-on-insulator substrate," *Journal of Vacuum Science & Technology B*, Vol. 26, 1560, 2008.
85. Kurczveil, G., D. Liang, M. Fiorentino, and R. G. Beausoleil, "Robust hybrid quantum dot laser for integrated silicon photonics," *Optics Express*, Vol. 24, 16167–16174, 2016.

86. Kurczveil, G., C. Zhang, A. Descos, D. Liang, M. Fiorentino, and R. G. Beausoleil, "On-chip hybrid silicon quantum dot comb laser with 14 error-free channels," *Proc. IEEE International Semiconductor Laser Conference (ISLC)*, 1–2, 2018.
87. Nguyen, H. C., Y. Sakai, M. Shinkawa, N. Ishikura, and T. Baba, "10 Gb/s operation of photonic crystal silicon optical modulators," *Optics Express*, Vol. 19, No. 14, 13000–13007, 2011.
88. Terada, Y., K. Kondo, R. Abe, and T. Baba, 'Full C-band Si photonic crystal waveguide modulator," *Optics Letters*, Vol. 42, No. 24, 5110–5112, 2017.
89. Shakoor, A., K. Nozaki, E. Kuramochi, K. Nishiguchi, A. Shinya, and M. Notomi, "Compact 1D-silicon photonic crystal electro-optic modulator operating with ultra-low switching voltage and energy," *Optics Express*, Vol. 22, No. 23, 28623–28634, 2014.
90. Zhang, J., X. Leroux, E. Durán-Valdeiglesias, C. Alonso-Ramos, D. Marris-Morini, L. Vivien, S. He, and E. Cassan, "Generating Fano resonances in a single-waveguide silicon nanobeam cavity for efficient electro-optical modulation," *ACS Photonics*, Vol. 5, No. 11, 4229–4237, 2018.
91. Marshall, O., M. Hsu, Z. Wang, B. Kunert, C. Koos, and D. van Thourhout, "Heterogeneous integration on silicon photonics," *Proceedings of the IEEE*, Vol. 106, No. 12, 2258–2269, 2018.
92. Heck, M. J., H.-W. Chen, A.-W. Fang, B. R. Koch, D. Liang, H. Park, M. N. Sysak, and J. E. Bowers, "Hybrid silicon photonics for optical interconnects," *IEEE Journal of Selected Topics in Quantum Electronics*, Vol. 17, No. 2, 333–346, 2010.
93. Alloatti, L., R. Palmer, S. Diebold, K. P. Pahl, B. Chen, R. Dinu, M. Fournier, J. M. Fedeli, T. Zwick, W. Freude, and C. Koos, "100 GHz silicon-organic hybrid modulator," *Light: Science & Applications*, Vol. 3, No. 5, e173, 2014.
94. Hu, Y., M. Pantouvaki, J. Van Campenhout, S. Brems, I. Asselberghs, C. Huyghebaert, P. Absil, and D. van Thourhout, "Broadband 10 Gb/s operation of graphene electro-absorption modulator on silicon," *Laser & Photonics Reviews*, Vol. 10, No. 2, 307–316, 2016.
95. Abel, S., F. Eltes, J. E. Ortmann, A. Messner, P. Castera, T. Wagner, D. Urbonas, A. Rosa, A. M. Gutierrez, D. Tulli, P. Ma, B. Baeuerle, A. Josten, W. Heni, D. Caimi, L. Czornomaz, A. A. Demkov, J. Leuthold, P. Sanchis, and J. Fompeyrine, "Large Pockels effect in micro- and nanostructured barium titanate integrated on silicon," *Nature Materials*, Vol. 18, 42–47, 2019.
96. Liang, D., G. Kurczveila, X. Huang, C. Zhang, S. Srinivasan, Z. Huang, M. A. Seyedi, K. Norris, M. Fiorentino, J. E. Bowers, and R. G. Beausoleil, "Heterogeneous silicon light sources for datacom applications," *Optical Fiber Technology*, Vol. 44, 43–52, 2018.
97. He, M., M. Xu, Y. Ren, J. Jian, Z. Ruan, Y. Xu, S. Gao, S. Sun, X. Wen, L. Zhou, L. Liu, and X. Cai, "High-performance hybrid silicon and lithium niobate Mach-Zehnder modulators for 100 Gbit s^{-1} and beyond," *Nature Photonics*, Vol. 13, No. 5, 359–364, 2019.
98. Roelkens, G., L. Liu, D. Liang, R. Jones, A. Fang, B. Koch, and J. E. Bowers, "III-V/silicon photonics for on-chip and intra-chip optical interconnects," *Laser & Photonics Reviews*, Vol. 4, No. 6, 751–779, 2010.
99. Tang, Y., J. D. Peters, and J. E. Bowers, "Over 67 GHz bandwidth hybrid silicon electroabsorption modulator with asymmetric segmented electrode for 1.3 μm transmission," *Optics Express*, Vol. 20, No. 10, 11529–11535, 2012.
100. Abbasi, A., J. Verbist, L. A. Shiramin, M. Verplaetse, T. de Keulenaer, R. Vaernewyck, R. Pierco, A. Vyncke, X. Yin, G. Torfs, and G. Morthier, "100-Gb/s electro-absorptive duobinary modulation of an InP-on-Si DFB laser," *IEEE Photonics Technology Letters*, Vol. 30, No. 12, 1095–1098, 2018.
101. Chen, K., Q. Huang, J. Zhang, J. Cheng, X. Fu, C. Zhang, K. Ma, Y. Shi, D. van Thourhout, G. Roelkens, L. Liu, and S. He, "Wavelength-multiplexed duplex transceiver based on III-V/Si hybrid integration for off-chip and on-chip optical interconnects," *IEEE Photonics Journal*, Vol. 8, No. 1, 7900910, 2016.
102. Huang, Q., Y. Wu, K. Ma, J. Zhang, W. Xie, X. Fu, Y. Shi, K. Chen, J.-J. He, D. van Thourhout, G. Roelkens, L. Liu, and S. He, "Low driving voltage band-filling-based III-V-on-silicon electroabsorption modulator," *Applied Physics Letters*, Vol. 108, No. 14, 141104, 2016.
103. Chen, H.-W., J. D. Peters, and J. E. Bowers, "Forty Gb/s hybrid silicon Mach-Zehnder modulator with low chirp," *Optics Express*, Vol. 19, No. 2, 1455–1460, 2011.

104. Han, J.-H., F. Boeuf, J. Fujikata, S. Takahashi, S. Takagi, and M. Takenaka, "Efficient low-loss InGaAsP/Si hybrid MOS optical modulator," *Nature Photonics*, Vol. 11, No. 8, 486–490, 2017.

105. Hiraki, T., T. Aihara, K. Hasebe, K. Takeda, T. Fujii, T. Kakitsuka, T. Tsuchizawa, H. Fukuda, and S. Matsuo, "Heterogeneously integrated III-V/Si MOS capacitor Mach-Zehnder modulator," *Nature Photonics*, Vol. 11, No. 8, 482–485, 2017.

106. Liang, D., X. Huang, G. Kurczveil, M. Fiorentino, and R. G. Beausoleil, "Integrated finely tunable microring laser on silicon," *Nature Photonics*, Vol. 10, 719–722, 2016.

107. Liang, D., C. Zhang, A. Roshan-Zamir, K. Yu, C. Li, G. Kurczveil, Y. Hu, W. Shen, M. Fiorentino, S. Kumar, S. Palermo, and R. Beausoleil, "A fully-integrated multi-λ hybrid DML transmitter," *Optical Fiber Communications Conference and Exposition (OFC)*, Th3B.5, 2018.